JGR Oceans

RESEARCH ARTICLE
10.1029/2023JC019651

Hydrodynamic Control of Sediment-Water Fluxes: Consistent Parameterization and Impact in Coupled Benthic-Pelagic Models

L. Umlauf[1], K. Klingbeil[1], H. Radtke[1], R. Schwefel[2], J. Bruggeman[3,4], and P. Holtermann[1]

[1]Leibniz Institute for Baltic Sea Research, Warnemuende, Germany, [2]Leibniz Institute for Freshwater Ecology and Inland Fisheries, Berlin, Germany, [3]Bolding & Bruggeman ApS, Asperup, Denmark, [4]Plymouth Marine Laboratory, Plymouth, UK

Abstract Benthic oxygen dynamics and the exchange of oxygen and other solutes across the sediment-water interface play a key role for the oxygen budget of many limnic and shallow marine systems. The sediment-water fluxes are largely determined by two factors: sediment biogeochemistry and the thickness of the diffusive boundary layer that is determined by near-bottom turbulence. Here, we present a fully coupled benthic-pelagic modeling system that takes these processes and their interaction into account, focusing especially on the modulation of the sediment-water fluxes by the effects of near-bottom turbulence and stratification. We discuss the special numerical methods required to guarantee positivity and mass conservation across the sediment-water interface in the presence of rapid element transformation, and apply this modeling system to a number of idealized scenarios. Our process-oriented simulations show that near-bottom turbulence provides a crucial control on the sediment-water fluxes, the oxygen penetration depth, and the re-oxidation of reduced compounds diffusing upward from the deeper benthic layers especially on time scales of a few days, characterizing oceanic tides, internal seiching motions in lakes, and mesoscale atmospheric variability. Our results also show that the response of benthic-pelagic fluxes to rapid changes in the forcing conditions (e.g., storm events) can only be understood with a fully coupled modeling approach.

Plain Language Summary Oxygen is one of the most relevant ecosystem parameters in marine systems and in lakes. In shallow systems, the overall oxygen budget is often controlled by the sedimentary oxygen demand, and it is therefore crucial to account for the exchange of oxygen and other solutes between the sediment and the water column. In this context, a thin (millimeter-scale) "diffusive sublayer," located immediately above the sediment surface, is known to play an especially important role as it may form a bottleneck for the solute exchange. As the thickness of this sublayer is controlled by hydrodynamic processes, sediment-water fluxes are affected by complex feedbacks between physical and biogeochemical processes. Here, we describe a fully coupled numerical modeling system that takes these feedback mechanisms into account, including advanced numerical methods guaranteeing that the total mass of all solutes is conserved (even if these are transformed) and that their concentrations do not become negative. Using a series of idealized examples, it is shown that near-bottom hydrodynamic processes have an important impact on the sediment-water fluxes, the depth to which oxygen penetrates into the upper sediment layers, and the re-oxidation of reduced chemical compounds in the sediments. These feedbacks are particularly important for processes with time scales of a few days, like ocean tides, internal oscillations in lakes, and short-term atmospheric disturbances (e.g., storm events).

Key Points:

- First fully coupled benthic-pelagic modeling system accounting for the effects of near-bottom turbulence on sediment-water solute fluxes
- Hydrodynamic effects control benthic biogeochemistry and fluxes especially on time scales of a few days, and during extreme events
- New numerical methods that guarantee mass conservation and positivity across the sediment-water interface

Supporting Information:

Supporting Information may be found in the online version of this article.

Correspondence to:

L. Umlauf,
lars.umlauf@io-warnemuende.de

Citation:

Umlauf, L., Klingbeil, K., Radtke, H., Schwefel, R., Bruggeman, J., & Holtermann, P. (2023). Hydrodynamic control of sediment-water fluxes: Consistent parameterization and impact in coupled benthic-pelagic models. *Journal of Geophysical Research: Oceans*, *128*, e2023JC019651. https://doi.org/10.1029/2023JC019651

Received 20 JAN 2023
Accepted 4 JUN 2023

Author Contributions:

Conceptualization: L. Umlauf, H. Radtke, R. Schwefel, P. Holtermann
Formal analysis: L. Umlauf, K. Klingbeil, P. Holtermann
Investigation: L. Umlauf
Methodology: L. Umlauf, K. Klingbeil, H. Radtke, R. Schwefel, J. Bruggeman, P. Holtermann
Software: K. Klingbeil, H. Radtke, J. Bruggeman, P. Holtermann

1. Introduction

The biogeochemistry of shallow marine systems, estuaries, and lakes is often controlled by benthic processes, mediated by the sediment-water fluxes of oxygen, nutrients, and other dissolved compounds (Glud, 2008). It is known that these fluxes are modulated by near-bottom turbulence, modifying the thickness of the diffusive boundary layer (DBL) and thus regulating the diffusive transfer of solutes across the sediment-water interface. Field studies based on oxygen microsensors in marine systems (e.g., Glud, 2008; Gundersen & Jorgensen, 1990; Wang et al., 2016) and various types of lakes (Bryant, Lorrai, et al., 2010; Lorke et al., 2003; Schwefel et al., 2017) have shown that fluctuations in near-bottom current speeds (and thus turbulence) due to tides, internal-wave motions, and other effects, are reflected in variations of the DBL thickness and hence benthic oxygen fluxes. Laboratory experiments (Hondzo, 1998; Inoue & Nakamura, 2009; Steinberger & Hondzo, 1999), near-bottom oxygen

Validation: L. Umlauf, K. Klingbeil, P. Holtermann
Visualization: L. Umlauf, P. Holtermann
Writing – original draft: L. Umlauf, P. Holtermann
Writing – review & editing: L. Umlauf, K. Klingbeil, H. Radtke, R. Schwefel, P. Holtermann

flux measurements based on the eddy covariance approach (Berg et al., 2022; Brand et al., 2008; Koopmans et al., 2021), and turbulence-resolving simulations (Calmet & Magnaudet, 1997; Scalo et al., 2012) support the finding that hydrodynamic effects often provide an important control on the sediment-water fluxes.

The above studies have shown that, for cohesive sediments, near-bottom turbulence affects the diffusive sediment-water flux f_c^b (positive upward here) of a solute c primarily by modifying the thickness δ_c of the DBL according to Fick's first law of diffusion:

$$f_c^b = -\nu_c \frac{c^\delta - c^b}{\delta_c}, \tag{1}$$

where c^b and c^δ are the solute concentrations at the bottom (i.e., at the sediment-water interface) and the top of the DBL, respectively, and ν_c is the molecular diffusivity of the solute. While it is, at least conceptually, straightforward to evaluate Equation 1 based on high-resolution microsensor data, the integration of this expression in numerical models is complicated by the various feedback mechanisms between the key parameters c^b, c^δ, and δ_c. Especially the effect of fluctuations in the DBL thickness, δ_c, is at the moment not taken into account even in advanced benthic-pelagic biogeochemical models (Brigolin et al., 2011; Butenschön et al., 2016; Fennel et al., 2013; Lemmen et al., 2018; Sohma et al., 2018). The description of these physically induced feedbacks, which will be the central topic of this work, requires a fully coupled benthic-pelagic modeling approach, including a physically sound description of the interfacial fluxes, accounting for hydrodynamic effects, and robust numerical methods that guarantee positivity and mass conservation. To our knowledge, such a combined approach has not yet been described.

Nevertheless, valuable insights about the role of hydrodynamics have been gained with more simple models, focusing on special aspects of the problem. Based on mathematical solutions for the benthic oxygen profiles for the special case of a constant aerobic respiration rate in the upper part of the benthic layer (Bouldin, 1968), a series of studies has attempted to determine the conditions under which the DBL may constitute a bottle-neck for the sediment-water fluxes (e.g., Hall et al., 1989; Higashino et al., 2004; Nakamura & Stefan, 1994). Jørgensen and Boudreau (2001) pointed out, however, that these studies, only considering aerobic respiration in a thin oxic layer below the sediment-water interface, may lead to erroneous conclusions about the role of the DBL as they ignore the reoxidation of reduced compounds like Mn^{2+}, Fe^{2+}, NH_4^+, H_2S, etc., diffusing upward from the deeper benthic layers. Based on a simple analytical solution describing sulfide reoxidation at the base of the oxic layer as the only relevant benthic oxygen sink, Jørgensen and Boudreau (2001, page 232) showed that the benthic oxygen demand is exclusively determined by the sulfide production rate. In this situation, the concentration difference $c^\delta - c^b$ in Equation 1 dynamically adjusts to compensate for any physically induced variability in δ_c, and the DBL can no longer by said to "control" the sediment-water fluxes. Numerical investigations with more complex diagenetic models have confirmed the important role of upward diffusion and reoxidation of reduced compounds for the response of the sediment-water fluxes with respect to variations of DBL thickness (Brand et al., 2009; Glud et al., 2007; Kelly Gerreyn et al., 2005). By combining data and biogeochemical modeling results, Glud (2008) and Glud et al. (2007) found that variations in DBL thickness, despite their limited effect on the long-term averaged fluxes, induce strong modifications in sediment-water fluxes on shorter time scales, from diurnal to seasonal. However, the benthic compartments in these modeling studies were forced by observed or prescribed pelagic parameters (e.g., near-bottom solute concentrations and current speeds), which eliminates any benthic-pelagic feedbacks.

The goal of our study is to identify and understand the basic hydrodynamically mediated mechanisms affecting the sediment-water fluxes, and to develop robust and reliable numerical methods for the implementation of these effects into coupled benthic pelagic models. As we are mainly interested in the role of the diffusive boundary layer, we ignore many other aspects of the hydrodynamic forcing, related, for example, to sediment resuspension and particle dynamics, which may be relevant in many marine systems but are not essential to understand the hydrodynamic feedback mechanisms studied here (and, in fact, may obscure them). For the same reason, we also ignore the effects of bioturbation, sediment accretion, conversion between pore water and liquids, and additional benthic processes that add complexity without providing additional insights into the processes we are interested in here. The modeling system developed in the following sections is, however, easily extendable to include any of these additional effects if required for a specific, more realistic application. The model equations and parameterizations for the sediment-water fluxes are described in Sections 2 and 3, followed by a detailed discussion of

the special numerical methods required to guarantee positivity and mass-conservation in coupled benthic-pelagic systems in Section 4. Model parameters, performance, and results for some process-oriented scenarios with increasing complexity are discussed in Sections 5 and 6 before we draw some conclusions in Section 7.

2. Transport Equations

2.1. Water Column

The horizontal velocity components u and v in the water column are computed based on one-dimensional transport equations of the form

$$\frac{\partial u}{\partial t} - fv = -g\frac{\partial \zeta}{\partial x} + \frac{\partial}{\partial z}\left((\nu_t + \nu)\frac{\partial u}{\partial z}\right), \tag{2}$$

$$\frac{\partial v}{\partial t} + fu = -g\frac{\partial \zeta}{\partial y} + \frac{\partial}{\partial z}\left((\nu_t + \nu)\frac{\partial v}{\partial z}\right), \tag{3}$$

where f denotes the Coriolis parameter, g the gravitational acceleration, and ν the molecular diffusivity of momentum. The surface elevation gradients, $\partial\zeta/\partial x$ and $\partial\zeta/\partial y$, are prescribed, and the vertical turbulent diffusivity of momentum, ν_t, is computed from a second-moment turbulence model that is described in more detail in Appendix A.

As the focus of our study is on processes near the sediment-water interface, we define the origin of our z-axis (pointing upward) at the sediment-water interface, implying that the water surface is located at $z = H$ (H is the water depth). As boundary conditions for Equations 2 and 3, we prescribe the surface stresses τ_x^s and τ_y^s, and compute the components of the bottom stresses vector $\boldsymbol{\tau}^b$ from a quadratic drag law of the form $\tau_x^b = -\rho_0 C_d |\boldsymbol{u}^b| u^b$ and $\tau_y^b = -\rho_0 C_d |\boldsymbol{u}^b| v^b$. Here, $\boldsymbol{u}^b$ denotes the velocity in the center of the lowermost grid cell, C_d the drag coefficient, and ρ_0 a constant reference density. For later use, the friction velocity u_* is defined as $u_*^2 = \tau^b/\rho_0$, where τ^b is the magnitude of the bottom stress. More details are provided in Sections 3 and 4.

The evolution of (potential) temperature, T, and salinity, S, is described according to

$$\frac{\partial T}{\partial t} = \frac{\partial}{\partial z}\left(\left(\nu_t^b + \nu_T\right)\frac{\partial T}{\partial z}\right) + \frac{r}{c_p}, \tag{4}$$

$$\frac{\partial S}{\partial t} = \frac{\partial}{\partial z}\left(\left(\nu_t^b + \nu_S\right)\frac{\partial S}{\partial z}\right), \tag{5}$$

where r is the heat supply per unit mass due to solar radiation, c_p the specific heat capacity, and ν_T and ν_S are the molecular diffusivities of heat and salt. The turbulent diffusivity, ν_t^b, is again computed from the second-moment turbulence model described in Appendix A. It is assumed to be identical for temperature, salinity, and all other scalar tracers. Temperature and salinity feedback on turbulence, and thus on the evolution of all predicted quantities, via their effect on stratification, quantified with the help of the (squared) buoyancy frequency, $N^2 \equiv \partial b/\partial z$, where $b = -g(\rho - \rho_0)/\rho_0$ is the buoyancy. The (potential) density ρ is computed from the TEOS-10 standard equation of state (http://teos-10.org, also see Feistel, 2012; Millero et al., 2008). As boundary conditions for Equation 4, we prescribe the surface heat flux q^s, whereas at the bottom we assume an insulating boundary ($q^b = 0$). The fluxes of salinity at the surface and at the bottom are assumed to be zero in all our simulations.

The water-column concentration c_ψ^w (per unit mass) of any dissolved tracer ψ (e.g., oxygen) follows from a reaction-transport equation of the form

$$\frac{\partial c_\psi^w}{\partial t} = \frac{\partial}{\partial z}\left(\left(\nu_t^b + \nu_\psi\right)\frac{\partial c_\psi^w}{\partial z}\right) + Q_\psi^w, \tag{6}$$

where ν_ψ denotes the corresponding molecular tracer diffusivity, and Q_ψ^w the sum of the source and sink terms.

As the goal of this study is the investigation of the basic hydrodynamic mechanisms that control the exchange of oxygen and other dissolved tracers across the sediment-water interface, we restrict ourselves to two types of tracers here: oxygen and a second tracer that we refer to as "oxygen demand units" (ODUs), representing the amount of oxygen required to re-oxidize reduced chemical compounds. Similarly, Soetaert et al. (1996a, 1996b)

suggested to use ODUs as a bulk representation for all reduced compounds other than ammonia whereas our more simpler model does not make this distinction. Based on the generic transport equation in Equation 6, the evolution of oxygen in the water column is modeled as

$$\frac{\partial c^w_{O2}}{\partial t} = \frac{\partial}{\partial z}\left(\left(\nu^b_t + \nu_{O2}\right) \frac{\partial c^w_{O2}}{\partial z} \right) - c^w_{O2} c^w_{OD} k_t, \tag{7}$$

whereas the evolution of the ODU concentration is described by an equation of the form

$$\frac{\partial c^w_{OD}}{\partial t} = \frac{\partial}{\partial z}\left(\left(\nu^b_t + \nu_{OD}\right) \frac{\partial c^w_{OD}}{\partial z} \right) - c^w_{O2} c^w_{OD} k_t. \tag{8}$$

The oxidation of ODUs is described here with the help of a standard second-order kinetic model, where the parameter k_t sets the reaction time scale. This parameter is assumed to be constant for simplicity in our idealized study although the numerical implementation would allow for a temperature dependency as in Radtke et al. (2019). For simplicity, we also ignore the dynamics of resuspended particles as well as any other direct oxygen or ODU source/sink terms in the water column (e.g., due to photosynthesis or respiration) as these processes are not essential to understand the basic hydrodynamic control mechanisms studied here. However, it would be straightforward to included any extra source and sink terms if required for a particular application.

The fluxes of oxygen and ODUs at the surface will be denoted as f^s_{O2} and f^s_{OD}, respectively, in the following. Here, we adjust f^s_{O2} exactly such that the surface oxygen concentration is always kept at the saturation level, computed as a function of temperature and salinity according Garcia and Gordon (1992). This implicitly assumes that the gas exchange with the atmosphere is uninhibited, which is a simple but sufficient model for the purpose of this idealized study. As c^w_{OD} will be negligibly small in the oxygen-saturated near-surface region, we assume that the flux of ODUs across the surface vanishes: $f^s_{OD}(z = H) = 0$ (although this condition could be easily relaxed if outgassing of ODUs would be a relevant factor). The fluxes of oxygen and ODUs at the bottom, f^b_{O2} and f^b_{OD}, depend on both the hydrodynamic conditions near the sediment-water interface and the biogeochemistry of the benthic compartment. These processes are the central topic of our paper, and will therefore be described in detail in the following section.

2.2. Benthic Compartment

The evolution of the concentration c^p_ψ (per unit pore water mass) of a tracer ψ dissolved in the pore water is modeled according to Boudreau (1997):

$$\phi \frac{\partial c^p_\psi}{\partial t} = \frac{\partial}{\partial z}\left(\phi \frac{\nu_\psi}{\theta^2} \frac{\partial c^p_\psi}{\partial z} \right) + \phi Q^p_\psi, \tag{9}$$

where ϕ is the (volumetric) porosity of the sediment and θ the tortuosity that represents the net effect of the curved diffusion path in a porous material. For simplicity, sediment accretion is ignored in our study. The sum of the sources and sinks of the tracer is denoted as Q^p_ψ. Here, consistent with Equations 7 and 8, we only consider oxygen and ODUs as relevant tracers. Following Equation 9, the transport equation for the porewater oxygen concentration can be expressed as

$$\phi \frac{\partial c^p_{O2}}{\partial t} = \frac{\partial}{\partial z}\left(\phi \frac{\nu_{O2}}{\theta^2} \frac{\partial c^p_{O2}}{\partial z} \right) - \phi S_{O2} \mathcal{H}\left(c^p_{O2}\right) - \phi c^p_{O2} c^p_{OD} k_t, \tag{10}$$

whereas the ODU evolution is described as

$$\phi \frac{\partial c^p_{OD}}{\partial t} = \frac{\partial}{\partial z}\left(\phi \frac{\nu_{OD}}{\theta^2} \frac{\partial c^p_{OD}}{\partial z} \right) + \phi S_{OD}\left(1 - \mathcal{H}\left(c^p_{O2}\right)\right) - \phi c^p_{O2} c^p_{OD} k_t, \tag{11}$$

where we used the same second-order kinetics as in Equations 7 and 8 to describe the re-oxidation of reduced compounds. The source/sink terms S_{O2} and S_{OD} describe the porewater consumption of oxygen and the production of ODUs by remineralization of organic matter, respectively. In our model, these constant rates are multiplied by the Heaviside function, $\mathcal{H}(x)$, which follows the usual definition that $\mathcal{H}(x) = 1$ for $x > 0$ and $\mathcal{H}(x) = 0$ otherwise.

According to Equations 10 and 11, this implies that oxygen is consumed at a constant rate, S_{O2}, as long as it is available $\left(c^p_{O2} > 0\right)$, and otherwise ODUs will be produced at the constant rate S_{OD}. Microorganisms will preferentially use dissolved oxygen for the mineralization process as this is the energetically most efficient choice. If oxygen becomes unavailable, other substances (nitrate, manganese and iron oxides, sulfate) will be used as alternative electron acceptors, thereby converting them to their reduced forms (ammonium, manganese-II and iron-II, hydrogen sulfide). Finally, methane will be produced, reducing the carbon itself. Our ODU tracer is thought to represent the bulk effect of (the most relevant of) these reduced compounds, which is similar to the approach used by Soetaert et al. (1996a, 1996b). ODUs will typically diffuse upward and become re-oxidized in the presence of dissolved oxygen. This secondary reaction acts as a non-conservative sink term in all tracer transport equations, reducing the concentration of both oxygen and ODUs at the same rate. For simplicity, we ignore the additional complexities of bioturbation, solid-liquid interactions, sediment accretion, etc., that do not form an essential component of the hydrodynamic feedback mechanisms we wish to study here.

3. Sediment-Water Fluxes

At the sediment-water interface, oxygen and ODUs are diffusively exchanged between the benthic compartment, represented by Equations 10 and 11, and the water column:

$$f^b_{O2} = -\phi \frac{\nu_{O2}}{\theta^2} \frac{\partial c^p_{O2}}{\partial z}, \quad f^b_{OD} = -\phi \frac{\nu_{OD}}{\theta^2} \frac{\partial c^p_{OD}}{\partial z} \quad \text{at } z = 0, \tag{12}$$

where f^b_{O2} and f^b_{OD} denote the diffusive fluxes per unit mass. Tracer fluxes at the lower edge of the benthic compartment, $z = -D$, are set to zero (here, D denotes the thickness of the benthic layer). Note that all fluxes are positive into the positive z-direction (i.e., positive upward).

3.1. Law of the Wall for Tracers

The sediment-water fluxes are determined by a complex interaction of the sediment biogeochemistry and the turbulent processes near the sediment-water interface. The latter are determined by well-known similarity solutions that are valid for high Reynolds number flows inside a near-bottom region with approximately constant fluxes (Pope, 2000). The vertical flux f^b_c (positive upward) of any tracer c (here: oxygen and ODUs) in this region corresponds, by definition, to the sediment-water flux, respectively.

Similar to the well-known logarithmic bottom layer for the velocity in Equation A5, Kader and Yaglom (1972) and Yaglom and Kader (1974) showed that, inside the constant flux region, also the profile of any tracer c follows a logarithmic behavior that, in our notation, can be written as

$$\frac{c^b - c}{c_*} = \frac{Sc_t}{\kappa} \ln \frac{z + z_0}{z_0} + \beta, \tag{13}$$

where c^b denotes the value of c directly at the sediment-water interface, $c_* = f^b_c / u_*$ the so-called friction (or flux) concentration, and $Sc_t = \nu_t / \nu^b_t$ the turbulent Schmidt number that Kader and Yaglom (1972) and Yaglom and Kader (1974) assumed to be constant. Finally, β denotes an unknown transfer function that essentially depends on the molecular Schmidt number, $Sc = \nu / \nu_c$, and the roughness properties of the bottom (see Appendix B).

The parameter z_0 appearing in Equation 13 is a length scale related to the bottom roughness. For a hydrodynamically smooth bottom, z_0 scales with the viscous sublayer thickness: $z_0 = \nu / u_* \exp(-\kappa B)$, which, using the standard values for the model parameters $\kappa \approx 0.4$ and $B \approx 5.5$, can also be written as $z_0 \approx 0.1 \nu / u_*$ (Pope, 2000). For a hydrodynamically rough bottom, z_0 is determined by the scale k_s of the bottom roughness elements: $z_0 = k_s \exp(-\kappa B')$, where B' is a model parameter. For $B' \approx 8.5$ (Pope, 2000), this yields the frequently used relation $z_0 \approx k_s / 30$. According to Kader (1981), a bottom with $k^+_s = k_s u_* / \nu < 3$ (or, equivalently, $z^+_0 = z_0 u_* / \nu < 0.1$) is hydrodynamically smooth, whereas a hydrodynamically rough bottom is characterized by $k^+_s > 100$ (or $z^+_0 > 3$).

It can be shown (see Appendix A) that the logarithmic near-bottom distributions for both momentum in Equation A5 and tracers in Equation 13 are exact solutions of our model equations. The model is therefore in perfect agreement with the wall-layer distributions suggested on theoretical grounds by Kader and Yaglom (1972) and Yaglom and Kader (1974). Note that this will be the case also for any other turbulence model that predicts a turbulent diffusivity profile as in Equation A7 with a constant turbulent Schmidt number Sc_t.

As our study will largely focus on the fundamental properties of the tracer equations and their numerical implementation, the details of the model for β are of secondary importance here. All our simulations will therefore rely on the simplified expression $\beta = 14.28\, Sc^{2/3}$, derived in Equation B2, which is applicable for a hydrodynamically smooth bottom and $Sc \to \infty$. Consistent with this model, we compute z_0 here and in Equation A5 based on the relation $z_0 = \nu/u_* \exp(-\kappa B)$, valid for a smooth bottom (see above).

3.2. Transfer Functions

From Equation A5, it is easy to show that the bottom momentum flux (or the bottom stress) can be written compactly as

$$\frac{\tau_b}{\rho_0} = u_*^2 = C_d |\boldsymbol{u}|^2, \tag{14}$$

with a quadratic drag coefficient defined as

$$C_d(z) = \left(\frac{1}{\kappa} \ln \frac{z + z_0}{z_0} \right)^{-2}. \tag{15}$$

It should be recalled that, for the smooth case, z_0 depends on u_*, such that a numerical iteration technique is required to solve the non-linear equation in Equation 14.

Similarly, the sediment-water flux f_c^b of a tracer c can be computed by re-arranging Equation 13 in the following form:

$$f_c^b = u_* r_c \left(c^b - c \right), \tag{16}$$

where the $u_* r_c$ can be interpreted as a transfer velocity, computed based on the transfer coefficient

$$r_c(z) = \left(\frac{Sc_t}{\kappa} \ln \frac{z + z_0}{z_0} + \beta \right)^{-1}. \tag{17}$$

Note that, different from the fixed "bulk" concentration typically assumed in transfer laws of the form in Equation 16 (see Boudreau, 1997), both the tracer concentration c and the transfer coefficient r_c appearing in Equation 16 are precisely defined functions of z. Especially for tracers with small molecular Schmidt/Prandtl number, that is, when β is small and the logarithmic component in Equation 17 thus becomes relevant, model results become grid dependent if this dependency on z is not taken into account.

For solutes with a large molecular Schmidt number Sc, on the other hand, we have $\beta \gg 1$ and thus $r_c \approx \beta^{-1}$ as the logarithmic term in Equation 17 will be negligible. Under this condition, and assuming that the concentration $c(z)$ above the DBL is approximately constant and equal to c_δ, equating Equations 1 and 16 yields an expression of the form

$$\delta_c \approx \frac{\nu_c}{u_* r_c} \approx \frac{\nu_c \beta}{u_*}, \tag{18}$$

which we will use below to diagnose the thickness of the DBL. Note that using the simplified expression for β in Equation B2, the diffusive boundary thickness in Equation 18 can be written as $\delta_c \propto Sc^{-1/3} \nu/u_*$, consistent with numerous expressions of the same form summarized in Boudreau (1997).

4. Numerics

The one-dimensional transport equations for momentum in Equations 2 and 3, temperature in Equation 4, and salinity in Equation 5 are solved as standard components of the General Ocean Turbulence Model (GOTM, see https://www.gotm.net), which forms the modeling environment used in our study. The turbulent diffusivities for momentum and tracers defined in Equation A1 are computed in GOTM from an algebraic second-moment turbulence closure model combined with two transport equations for the turbulence kinetic energy, Equation A2, and the dissipation rate, Equation A3, as explained in more detail in Appendix A. The numerical discretization

and implementation of these standard equations are described in (Umlauf et al., 2005), and are therefore only briefly summarized below. For the purpose of this study, GOTM was extended by including discretized versions of the transport equations for the biogeochemical tracers, Equations 7 and 8, and a benthic module, in which the transport equations for the pore water concentrations, Equations 10 and 11, are solved. For both the pelagic and the benthic compartments, we used a time splitting scheme to separate the vertical transport terms from the biogeochemical reactions based on the Framework for Aquatic Biogeochemical Models (FABM, see Bruggeman and Bolding (2014) and https://fabm.net). Details are described in the following.

4.1. Vertical Transport of Tracers

The vertical grids in the water column and benthic compartments consist of $k^w_{\max}$ and $k^p_{\max}$ vertical layers with thickness h_k, respectively. In the following, layers in the water column are numbered from $k = 1$ at the bottom to $k = k^w_{\max}$ for the uppermost layer just below the water surface. For the benthic compartment, layers are numbered from $k = -1$ (just below the sediment-water interface) to $k = -k^p_{\max}$ at the lower edge of the sediment compartment.

For a generic description of vertical transport in both the water column and the sediment compartment, and in view of a future extension of our numerical method to three-dimensional applications, we assign generalized "volumes" V_k to all grid cells. In the one-dimensional modeling context discussed here, we have $V_k = h_k$ for the water column, whereas for the benthic compartment, we additionally account for the reduction of the porewater volume due to porosity: $V_k = \phi_k h_k$. Similarly, we define horizontal interface "areas," $A_{k+1/2}$, between grid cells k and $k + 1$. In the simple one-dimensional context discussed here, we have $A_{k+1/2} = 1$ for the water column, whereas, for the benthic compartment, we again account for the effect of porosity: $A_{k+1/2} = \phi_{k+1/2}$. The effective area A_b of the sediment-water interface is given by $A_b = A_{1/2} = A_{-1/2} = \phi_{-1/2}$.

During each time step, we first update the transport equations for momentum in Equations 2 and 3, temperature in Equation 4, and salinity in Equation 5, and their boundary conditions, as described in detail in Umlauf et al. (2005). Then, as the first step of our operator splitting approach, the biogeochemical tracer concentrations are updated from their values c^n at time t^n to an intermediate time stage $c^\star$, taking into account only the effect of vertical transport. Using the generalized cell "volumes" and interface "areas" introduced above, our time stepping scheme for the vertical transport terms can be written as

$$V_k \frac{c^\star_k - c^n_k}{\Delta t} = -\left(A_{k+1/2} J_{k+1/2} - A_{k-1/2} J_{k-1/2}\right), \tag{19}$$

where Δt denotes the (constant) time step and $J_{k+1/2}$ the diffusive flux between grid cells k and $k + 1$. The latter is discretized from a semi-implicit scheme of the form

$$J_{k+1/2} = -\nu_{k+1/2}\left(\sigma \frac{c^\star_{k+1} - c^\star_k}{z_{k+1} - z_k} + (1-\sigma)\frac{c^n_{k+1} - c^n_k}{z_{k+1} - z_k}\right), \tag{20}$$

where z_k is the vertical position of the center of the kth layer, and $\nu_{k+1/2}$ the effective diffusivity at the interface. For the water column, $\nu_{k+1/2}$ corresponds to the sum of the molecular and turbulent diffusivities in Equations 7 and 8, whereas for the pore water equations in Equations 10 and 11, $\nu_{k+1/2}$ includes the θ^2 term to account for the effects of tortuosity. For a large diffusivity, a small layer thickness, and a large time step, only a fully implicit scheme with $\sigma = 1$ preserves non-negative tracer concentrations, $c^\star \geq 0$. We will therefore only use this type of time stepping scheme in the following.

4.2. Sediment-Water Fluxes

The water column and the benthic compartments are coupled via the tracer flux f^b_c at the sediment water interface. With f^b_c from Equation 16, the flux on the water side is given by

$$A_{1/2} J_{1/2} = f_{1/2} = u_* r_c(z_1)\left(c^b - c_1\right), \tag{21}$$

whereas a one-sided discretization of the flux on the sediment side yields:

$$A_{-1/2} J_{-1/2} = f_{-1/2} = -\phi_{-1/2} \frac{\nu_c}{\theta^2_{-1/2}} \frac{c^b - c_{-1}}{0.5 h_{-1}}. \tag{22}$$

As already noted in the context of Equation 17 above, the dependency of r_c on the position z_1 of the lowermost grid point in Equation 21 insures that our bulk model for the sediment-water fluxes is grid-independent. This is not the case for bulk models that assume a constant transfer coefficient.

Assuming continuity across the sediment-water interface, $f_{1/2} = f_{-1/2}$, Equations 21 and 22 can be combined into an equation for the tracer concentration at the interface,

$$c^b = \frac{u_* r_c(z_1) c_1 + \phi_{-1/2} \frac{\nu_c}{\theta^2_{-1/2} 0.5 h_{-1}} c_{-1}}{u_* r_c(z_1) + \phi_{-1/2} \frac{\nu_c}{\theta^2_{-1/2} 0.5 h_{-1}}}. \tag{23}$$

Based on Equations 22 and 23, the sediment-water flux can be written as a diffusive flux,

$$f_c^b(c_1, c_{-1}) = -A_b \nu_b \frac{c_1 - c_{-1}}{z_1 - z_{-1}}, \tag{24}$$

where the effective diffusivity at the sediment-water interface is

$$\nu_b = \nu_{1/2} = \nu_{-1/2} = \frac{u_* r_c(z_1) \frac{\nu_c}{\theta^2_{-1/2} 0.5 h_{-1}}}{u_* r_c(z_1) + \phi_{-1/2} \frac{\nu_c}{\theta^2_{-1/2} 0.5 h_{-1}}} (z_1 - z_{-1}). \tag{25}$$

Integrating Equation 25 into Equations 19 and 20, a coupled tridiagonal system of equations for the combined pelagic and benthic compartments can be derived. While it would be possible to solve this system directly, we prefer to split it into two tridiagonal subsystems for the pelagic and benthic compartments, respectively, to allow for a better modularization of the code, in particular regarding the possibility to use different time steps for both compartments (although this option is currently not used in our implementation). In each of these subsystems, $f_c^b\left(c_1^n, c_{-1}^n\right)$ is applied as a Neumann boundary condition at the sediment-water interface. In order to avoid negative tracer concentrations, any outgoing boundary flux is limited by an implicit Patankar-type source term discretization (Patankar, 1980):

$$f_{1/2} = f_{-1/2} = \begin{cases} \left(c_1^\star / c_1^n\right) f_c^b & \text{for } f_c^b = f_c^b\left(c_1^n, c_{-1}^n\right) < 0, \\ \left(c_{-1}^\star / c_{-1}^n\right) f_c^b & \text{for } f_c^b = f_c^b\left(c_1^n, c_{-1}^n\right) > 0. \end{cases} \tag{26}$$

In practice, the application of Equation 26 requires that the sequence in which the linear systems for the pelagic and benthic compartments are solved, respectively, is determined at run time, depending on the direction of the sediment-water flux $f_c^b\left(c_1^n, c_{-1}^n\right)$ at the current time step: the system for the donating compartment is always solved first, and the Patankar-limited boundary flux is then diagnosed and applied to the receiving compartment to guarantee mass conservation. Note that this component of our numerical scheme is essential to guarantee positivity and stability.

4.3. Biogeochemical Reactions

After integrating the vertical transport terms for both compartments according to Equations 19 and 20, the time step is completed by including the effects of biogeochemical reactions according to:

$$\frac{c_k^{n+1} - c_k^\star}{\triangle t} = Q_k, \tag{27}$$

where Q_k denotes the sum of the source and sink terms appearing on the right hand sides of the tracer transport equations. Numerically, we use the positive Euler-Forward method described by Radtke and Burchard (2015) to solve Equation 27. This is a simple clipping method that avoids negative concentrations. First, the source and sink terms for the three types of processes appearing in the tracer equations are computed: oxygen consumption in the sediment, ODU production in the sediment, and second-order reactions between oxygen and ODUs. A simple Euler-Forward integration is typically done to update the concentrations. However, if this approach turns out to locally produce negative oxygen or ODU concentrations, we split the time step. We first integrate over a

sub-timestep, whose length is chosen to yield a tracer concentration (for either ODUs or oxygen) of exactly zero. Then, we switch off all processes that consume this tracer. If it is oxygen consumption that we switched off, we activate ODU production instead, since the grid cell is now anoxic. With these modified process rates, we finally integrate over the remaining sub-timestep, again using an Euler-forward scheme. It is straightforward to generalize this approach to an arbitrary number of tracers (Radtke & Burchard, 2015).

5. Conservation Properties and Parameters

5.1. Conservation Properties

The tracer concentrations in the water column, c^w_{O2} and c^w_{OD}, and the pore water, c^p_{O2} and c^p_{OD}, are no conserved quantities because the re-oxidization of ODUs in regions with overlapping non-zero concentrations represents a sink term for both oxygen and ODUs. However, the concentration differences, $c^w_{O2} - c^w_{OD}$ and $c^p_{O2} - c^p_{OD}$, are not affected by this process. This can be easily shown by computing the difference of the corresponding transport equations for the water column, Equations 7 and 8, and the benthic compartment, Equations 10 and 11, respectively. Integrating the resulting difference equations across the water column of depth H and the benthic layer of thickness D, respectively, yields:

$$\frac{\mathrm{d}}{\mathrm{d}t}\int_0^H \left(c^w_{O2} - c^w_{OD}\right)\mathrm{d}z = -f^s_{O2} + \left(f^b_{O2} - f^b_{OD}\right), \tag{28}$$

$$\frac{\mathrm{d}}{\mathrm{d}t}\int_{-D}^0 \phi\left(c^p_{O2} - c^p_{OD}\right)\mathrm{d}z = -\int_{-D}^0 \phi\left[S_{O2}\mathcal{H}\left(c^p_{O2}\right) + S_{OD}\left(1 - \mathcal{H}\left(c^p_{O2}\right)\right)\right]\mathrm{d}z - \left(f^b_{O2} - f^b_{OD}\right), \tag{29}$$

where we used the boundary conditions in Equation 12 and assumed, as already noted above, that the ODU flux at the oxygen-saturated water surface is negligible, and that all fluxes vanish at the lower edge of the benthic compartment, $z = -D$. We will refer to the concentration differences, $c^w_{O2} - c^w_{OD}$ and $c^p_{O2} - c^p_{OD}$, as the "total" oxygen concentrations in the following, noting that negative total oxygen concentrations indicate the amount of oxygen required to completely re-oxidize available ODUs.

Assuming that the porosity, ϕ, is vertically constant and that the consumption rates are equal, $S_{O2} = S_{OD}$, which is a reasonable approximation in the context of our study as discussed in more detail below, Equation 29 can be further simplified to yield:

$$\frac{\mathrm{d}}{\mathrm{d}t}\int_{-D}^0 \phi\left(c^p_{O2} - c^p_{OD}\right)\mathrm{d}z = -\phi S_{O2} D - \left(f^b_{O2} - f^b_{OD}\right), \tag{30}$$

Under stationary conditions, adding Equations 28 and 30 yields $f^s_{O2} = -\phi S_{O2} D$, which has the simple interpretation that all oxygen consumed in the sediment has to enter the coupled sediment-water system via the surface. A similar relation can also be deduced from Equation 30 for the sediment-water fluxes (again for stationary conditions): $f^b_{O2} - f^b_{OD} = -\phi S_{O2} D$, suggesting that the total benthic oxygen demand is balanced by both an oxygen flux into, and an export of ODUs out of, the benthic compartment (although the former usually dominates, as shown below).

5.2. Parameters

Many of the parameters determining the sediment properties and biogeochemistry are not well constrained. A precise quantification of all parameters, however, is not required for our idealized study focusing on the basic mechanisms controlling the diffusive sediment-water fluxes. We will therefore largely rely on order-of-magnitude estimates here, and only investigate the sensitivity of our results with respect to changes in the most relevant parameters.

As the molecular diffusivities for oxygen and the majority of the relevant reduced substances are of the order of $10^{-9}\ \mathrm{m^2\ s^{-1}}$ (e.g., at 20°C: $0.7 \times 10^{-9}\ \mathrm{m^2\ s^{-1}}$ for Fe^{2+} and Mn^{2+}; $1.9 \times 10^{-9}\ \mathrm{m^2\ s^{-1}}$ for NH_4^+; and $2.4 \times 10^{-9}\ \mathrm{m^2\ s^{-1}}$ for O_2), we chose $\nu_{O2} = \nu_{OD} = 10^{-9}\ \mathrm{m^2\ s^{-1}}$ in the following. For the porosity, we chose a typical value of $\phi = 0.9$ and assume, for simplicity, $\theta = 1$ for the tortuosity, noting, however, that the numerical implementation allows for arbitrary distributions of both quantities.

An order-of-magnitude estimate for the consumption/production rates, S_{O2} and S_{OD}, can be obtained from the simple assumption that the oxygen flux through the sediment-water interface is consumed in the benthic compartment, either by aerobic respiration or by the oxidation of ODUs. Various studies conducted in lakes (Brand et al., 2008; Bryant, Lorrai, et al., 2010; Bryant, McGinnis, et al., 2010; Lorke et al., 2003; Schwefel et al., 2017) and shallow marine

Table 1
Standard Model Parameters

Name	Description	Value	Unit
D	Thickness of benthic layer	0.05	m
ϕ	Porosity	0.9	m^3 (liquid)/m^3 (bulk)
θ	Tortuosity	1	
ν_{O2}	Molecular diffusivity of O_2	1×10^{-9}	$m^2\ s^{-1}$
ν_{OD}	Molecular diffusivity of ODUs	1×10^{-9}	$m^2\ s^{-1}$
k_t	Turnover rate	5×10^5	kg $mol^{-1}d^{-1}$
S_{O2}	Oxygen consumption rate	2.22×10^{-4}	mol $kg^{-1}d^{-1}$
S_{OD}	ODU production rate	2.22×10^{-4}	mol $kg^{-1}d^{-1}$
H	Water depth	10	m
τ_x^s	Surface stress	1×10^{-2}	Pa

systems (Berg et al., 2003; Holtappels et al., 2013, 2015) have shown that oxygen fluxes (per unit volume) are often of order 10 mmol m^{-2} d^{-1}, which, converted to the fluxes per unit mass used in our study, corresponds to $f^b_{O2} = 10^{-5}$ mol kg^{-1} m d^{-1}. As discussed in the context of Equation 30, for an oxic sediment-water interface, the stationary oxygen flux is largely determined by the integrated oxygen consumption rate in the sediment, $f^b_{O2} \approx -\phi S_{O2} D$, where we assumed that $S_{O2} = S_{OD}$. This implies that we assume organic carbon degradation to be independent of depth and equal under oxic and anoxic conditions (i.e., independent of the oxidant). This is clearly a strong assumption. In the supporting material, we have therefore discarded the assumption that $S_{O2} = S_{OD}$, and conducted additional experiments with $S_{O2} > S_{OD}$, which may be viewed as a simple representation of a vertically decaying remineralization rate. Figures S2 and S3 in the Supporting Information S1 show that, near the sediment-water interface, solute distributions, turnover rates, oxygen penetration depths, and benthic fluxes are only weakly affected even for large respiration ratios up to $S_{O2}/S_{OD} = 12.5$ (Figure S3 in the Supporting Information S1). As we only focus on hydrodynamically mediated feedback mechanisms near the sediment-water interface here, and wish to keep our model as simple as possible, we therefore believe that our assumption $S_{O2} = S_{OD}$ is justified for the purpose of our study.

For $\phi = 0.9$, the consumption rate S_{O2} can thus be estimated if f^b_{O2} and the thickness D of the active benthic layer are known. Using the above value for f^b_{O2}, and assuming $D = 0.05$ m, we find $S_{O2} = S_{OD} = 2.22 \times 10^{-4}$ mol kg^{-1} d^{-1}. As the reoxidation of ODUs is largely confined to a thin region close to the sediment-water interface, numerical sensitivity experiments have shown that varying D and $S_{O2} = S_{OD}$, while keeping their product constant, did not significantly affect benthic fluxes and turnover rates (one example for a two times larger benthic layer thickness of $D = 0.1$ m is shown in Figure S1 in the Supporting Information S1).

The parameter k_t, which sets the timescale for the oxidation of ODUs, strongly depends on the (combination of) reduced compounds thought to be represented by the ODUs (Boudreau, 1997). An order-of-magnitude estimate for k_t can be obtained by noting that the thickness of the oxic layer, D_{O2}, at the sediment surface is governed by a balance between downward diffusion and local oxygen demand by the reoxidation of reduced compounds (this implies that, for this estimate, we assume that aerobic respiration is negligible). Estimates for the diffusion and re-oxidation time scales are $T_D \sim D^2_{O2}/\nu_{O2}$ and $T_k \sim \left(k_t \bar{c}_{O2}\right)^{-1}$, respectively, where $\bar{c}_{O2}$ denotes a representative oxygen concentration that, for a well ventilated water column, is assumed to scale with the saturation concentration (a few times 10^{-3} mol kg^{-1}). Thus, for $T_D \sim T_k$, we have $k_t \sim \nu_{O2}/\left(D^2_{O2}\bar{c}_{O2}\right)$. Assuming the oxygen penetration depth is typically of the order of a few millimeters, we find a k_t of the order of a few times 10^5 kg $mol^{-1}d^{-1}$. Here, we choose $k_t = 5 \times 10^5$ kg $mol^{-1}d^{-1}$ for our basic scenarios, noting that the effect of other values is investigated in more detail below. All model parameters are summarized in Table 1.

6. Numerical Simulations

To test the robustness and reliability of our numerical scheme also under extreme conditions, we start our numerical investigations with an idealized setup, designed to reveal any deficiencies in the numerical methods and implementation. This model configuration includes a water column and a benthic compartment, both initialized with a strong oxygen deficit (large ODU concentrations) and gradually ventilated by the downward mixing of oxygen from the

surface. During the course of this numerical experiment, the redoxcline propagates downward through the entire water column, crosses the sediment-water interface, and finally merges into the upper part of the benthic compartment. The rapid oxidation of ODUs in the vicinity of the redoxcline poses a serious challenge to the numerical scheme especially during the transition of the redoxcline across the sediment-water interface, which would immediately reveal potential numerical shortcomings with respect to mass conservation, positivity, and stability.

The geometry for this idealized setup consists of an unstratified ($N = 0$) and non-rotating ($f = 0$) shallow water column ($H = 10$ m) with a hydrodynamically smooth bottom, and an underlying active benthic layer of $D = 0.05$ m thickness. Initially, both the water column and the porewater are anoxic $\left(c^w_{O2} = c^p_{O2} = 0\right)$ and characterized by a constant ODU concentration of $c^w_{OD} = c^p_{OD} = c^{max}_{OD}$, where $c^{max}_{OD} = 2.65 \times 10^{-3}$ mol kg^{-1}, is the maximum porewater concentration in the sediment after steady-state conditions have been reached (this initialization was chosen to accelerate the approach to steady-state conditions). At time $t = 0$, a constant wind stress of $\tau^s_x = 0.01$ Pa is applied ($\tau^s_y = 0$ in all our experiments), and the surface oxygen flux f^s_{O2} is adjusted at each time step to keep the surface oxygen concentration at the saturation level (here set to $c^w_{O2} = 3 \times 10^{-4}$ mol kg^{-1}), as explained at the end of Section 2.1 above. All other parameters correspond to those summarized in Table 1. The transport equations are discretized with a constant vertical resolution of $\Delta z = 0.1$ m for the water column, and, for the benthic compartment, with 50 vertical layers with thickness decreasing from 2.0×10^{-3} m at the lower edge of the benthic layer to 1.5×10^{-4} m at the sediment-water interface. A common time step of $\Delta t = 5$ s is used for both compartments. For these values, the solutions do not dependent significantly any more on the vertical resolution and time step.

6.1. Temporal Evolution

Although the turbulent surface layer entrains down to the bottom within approximately 3 hr in this example, oxygen concentrations in the water column remain close to zero throughout the first day (Figure 1a), while ODU concentrations gradually decay to zero (Figure 1c). In our example, this decay time scale is determined by the rate at which oxygen is mixed down into the suboxic zone (rather than by the re-oxidation rate), as discussed in more detail below. After approximately a day, the redoxcline crosses the sediment-water interface, and the uppermost part of the benthic layer becomes oxic (Figure 1b).

This thin oxic layer near the sediment surface reaches an approximately stationary thickness of a few millimeters already after a few days, whereas ODU concentrations in the lower part of the benthic layer (not shown in Figure 1d) continue to evolve for several weeks while gradually approaching stationary conditions. In our example, the adjustment time scale for the benthic ODU concentrations is determined by the diffusive time scale, $T_D = D^2/\nu_{OD} \approx 29$ days for the parameters in Table 1, consistent with the numerical simulations.

These adjustment processes are also reflected in the tracer concentrations and fluxes at the sediment-water interface. Figure 2a shows that shortly after all ODUs in the water column have been oxidized, oxygen concentrations in the center of the lowermost grid cell at $z = z_1$ (0.05 m above the sediment-water interface) start to rise, quickly reaching values near the saturation level at the surface (dashed line). Due to the large turbulent diffusivities in the water column, the small concentration difference between the surface and lowermost grid box (hardly discernible on the scale of the plot) is sufficient to drive a downward turbulent oxygen flux that compensates the benthic oxygen demand after approximately stationary conditions are reached.

Consistent with the flux model in Equation 21, oxygen fluxes into the sediment (Figure 2b) increase along with the increasing concentration contrast between the lowermost grid point and the sediment-water interface (blue and orange curves in Figure 2a) until they reach their steady-state values. Note that when stationary conditions are approached, the downward oxygen flux into the sediment (orange curve in Figure 2b) is slightly smaller than surface oxygen flux (in blue), pointing at a small but non-negligible ODU flux (in green) out of the sediment even under stationary conditions. Part of the oxygen entering the system through the surface is thus used to re-oxidize ODUs diffusing out of the sediment. For $t \to \infty$ (not shown), the surface oxygen flux (in blue) approaches to the long-term total benthic oxygen demand of 10 mmol m^{-2} d^{-1} (dashed line), as required by mass conservation.

At the bottom of the benthic compartment ($z = -D$), ODU concentrations (Figure 2a, in red) slowly increase due to ODU production up to a maximum value reached on day 4, when the effect of downward diffusing oxygen becomes relevant, and ODU concentrations start decreasing again until the long-term stationary limit c^{max}_{OD} is reached (not shown in the figure due the long diffusive adjustment time scale, see above).

Figure 3a shows that a stronger wind stress leads to a faster oxygenation of the water column and thus to an earlier onset of oxygen fluxes into the sediment. This suggests that the re-oxidation of ODUs in the water column is

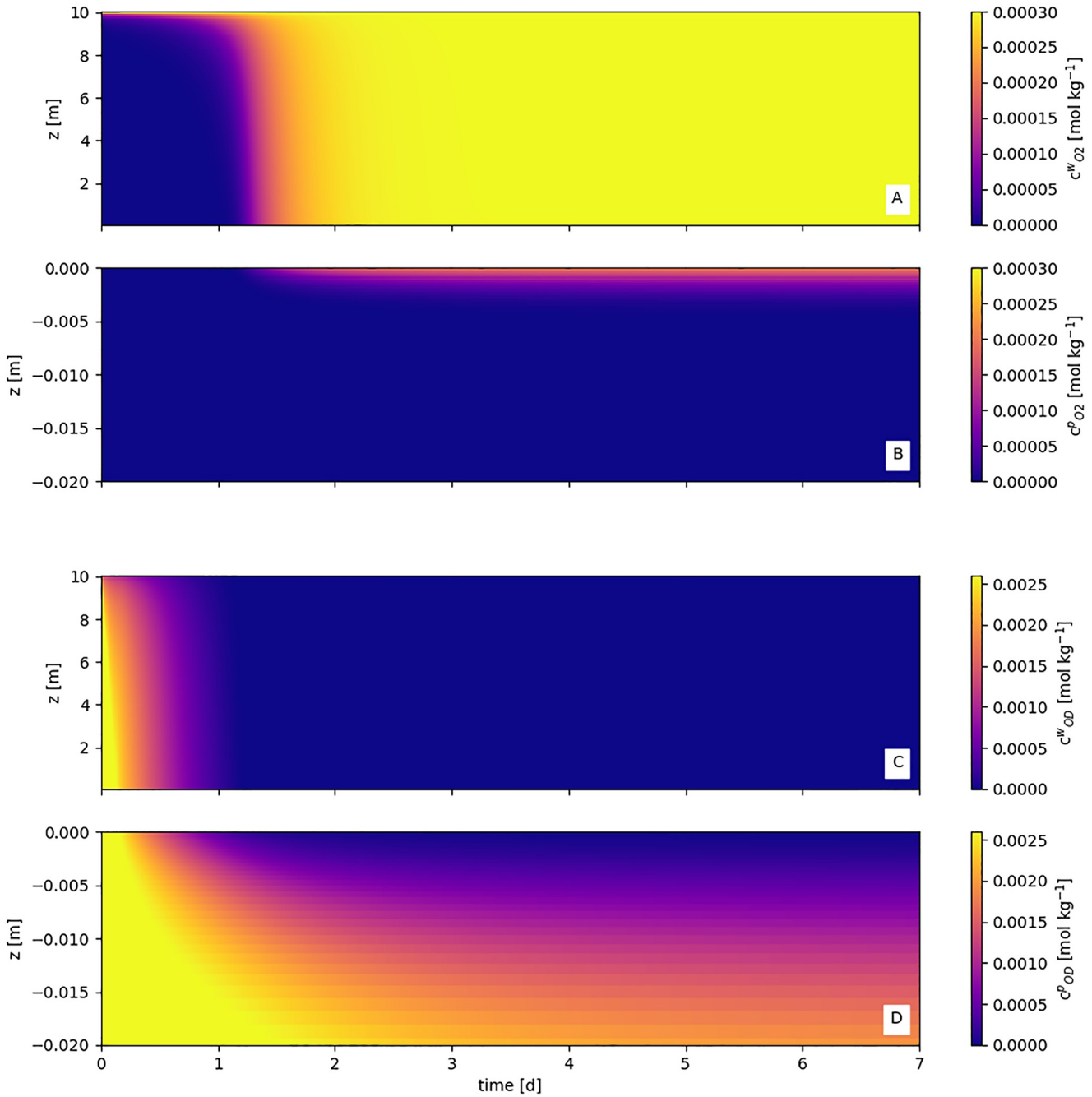

Figure 1. Evolution of oxygen concentrations (a) in the water column and (b) in the benthic compartment; and oxygen demand unit concentrations (c) in the water column and (d) in the benthic compartment. Note that only the upper 0.02 m of the active benthic layer with $D = 0.05$ m thickness are shown.

largely controlled by the downward turbulent transport of oxygen from the surface rather than by the value of the turnover rate k_t. A larger surface stress also leads to larger bottom currents, a larger bottom stress, and thus, according to Equation 18, a thinner DBL. This is reflected especially in the steady-state interface concentrations (Figure 3b), which, for increasing surface stress, gradually approach the saturation concentrations in the water column. For the largest wind stress, the DBL thickness, computed from Equation 18, has become so small ($\delta_{O2} = 0.18$ mm) that the interface concentration is within 94% of the saturation concentration.

Variations in near-bottom turbulence also control the magnitude of the sediment-water fluxes during the initial adjustment phase. Figure 3a shows that stronger turbulence leads to an initial overshooting of the sediment-water fluxes by more than 50% beyond the long-term benthic oxygen demand of 10 mmol m^{-2} d^{-1}. For the less turbulent

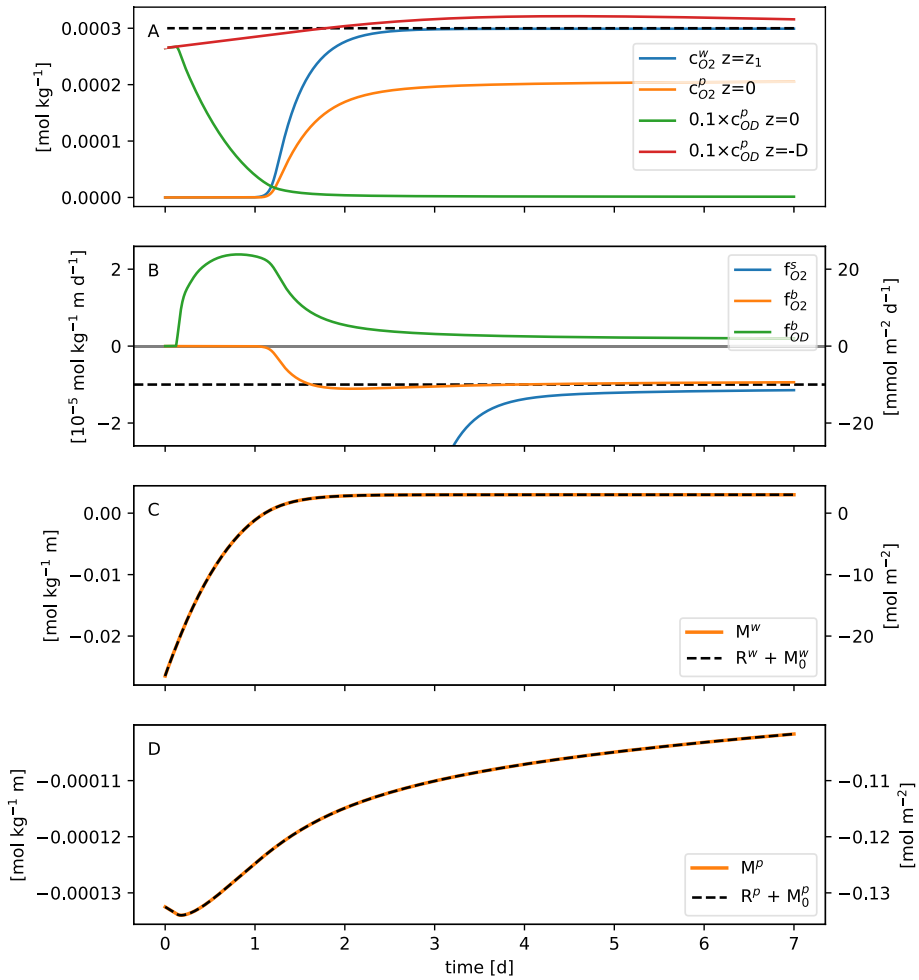

Figure 2. Temporal evolution of (a) oxygen and oxygen demand unit (ODU) concentrations at different vertical levels in the water column and benthic compartment (dashed line indicates the oxygen saturation concentration); (b) oxygen and ODU fluxes (positive upward, zero marked by gray line) at the surface and sediment-water interface (dashed line indicates the long-term benthic oxygen demand), (c) vertically integrated tracer budget for the water column according to Equation 31, and (d) vertically integrated tracer budget for the benthic compartment according to Equation 32. Note the different scales for oxygen and ODUs, respectively, in panel (a). In panels (b)–(d), for convenience, the left and right axes indicate tracer concentrations both per unit mass and per unit volume, respectively.

cases, a thicker DBL provides an increasingly important bottle neck for the transport of oxygen into the sediment during this initial phase, suggesting that the initial benthic "oxygen debt" is "repaid" over longer time scales (Glud, 2008). After approximately 1 week, however, all fluxes approach steady-state values close to total benthic oxygen demand of 10 mmol m^{-2} d^{-1}. The small differences in the these stationary sediment-water fluxes can again be attributed to the slightly different ODU fluxes from the sediment into the water column, as explained above.

6.1.1. Mass Conservation

To investigate the conservation properties of our numerical scheme, it is useful to integrate Equation 28 in time, showing that the amount $M^w(t)$ of "total" oxygen (see above) in the water column evolves according to

$$M^w(t) = \int_0^H \left(c^w_{O2} - c^w_{OD}\right) dz = R^w(t) + M^w_0, \tag{31}$$

where $M^w_0 = M^w(t = 0)$, and $R^w(t)$ is the time integral of the right hand side of Equation 28. Similarly, the amount $M^p(t)$ of "total" oxygen in the pore water can be computed from integrating Equation 30, yielding an expression of the form

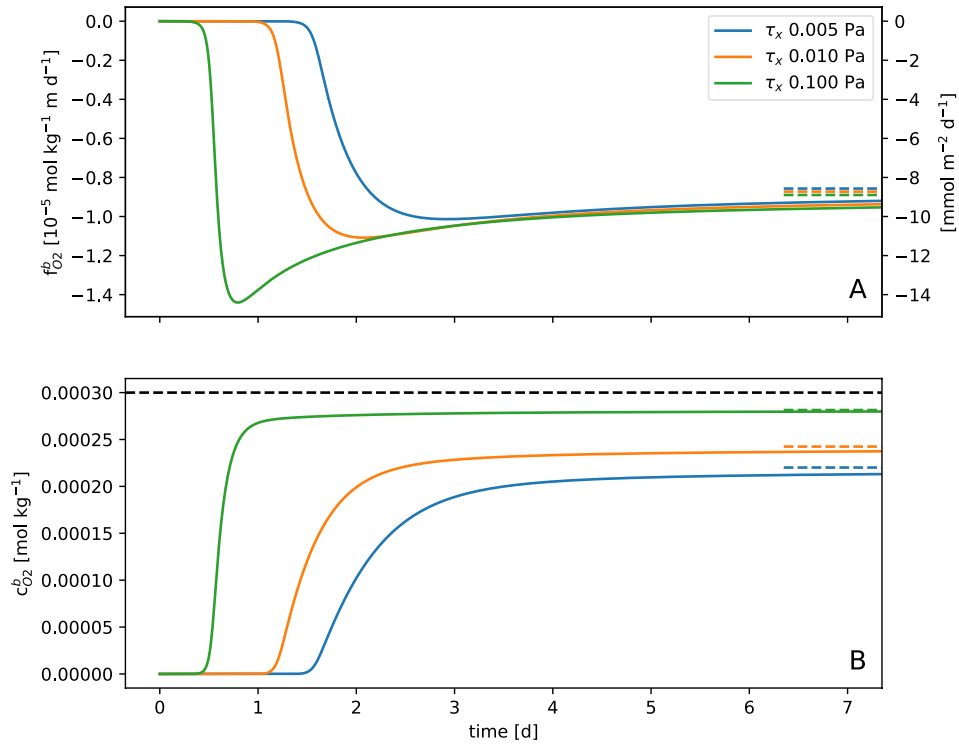

Figure 3. Temporal evolution of (a) sediment-water oxygen fluxes and (b) oxygen concentrations at the sediment-water interface for different values of the surface wind stress τ^s_x. The colored dashed lines indicate the steady-state values for $t \to \infty$, respectively. The black dashed line in (b) shows the saturation concentration. All other parameters as in Figures 1 and 2.

$$M^p(t) = \int_{-D}^{0} \left(c^p_{O2} - c^p_{OD}\right) dz = R^p(t) + M^p_0, \tag{32}$$

with the initial amount of tracer, M^p_0, and the time integral $R^p(t)$ of the right hand side of Equation 30.

Figures 2c and 2d, comparing the left and right-hand sides of Equations 31 and 32, respectively, show that our model reproduces these complex tracer budgets with perfect accuracy across the entire simulation period. Combined with the results above, we therefore conclude that our numerical approach is stable, conservative, and guarantees positivity even in this numerically challenging scenario with a redoxcline crossing the sediment-water interface.

6.1.2. Steady-State Solutions

After stationary conditions have been reached in the above examples, the solutions are characterized by vertically constant fluxes of momentum and tracers across the entire water column, respectively. For the velocity, this results into the well-known Couette-type flow structure with two logarithmic wall-layer layers near the surface and the bottom (see Pope, 2000). At the bottom, the non-dimensional velocity profile (Figure 4a) converges toward the characteristic logarithmic shape in Equation A5, and the turbulent diffusivity (Figure 4c) approaches the linear wall-layer solution in Equation A6. The vertical profile of the non-dimensional oxygen concentration (Figure 4b) is identical to that for momentum, except for a constant offset of magnitude β and a factor of order 1 due to the presence of the turbulent Schmidt number in Equation 13. For tracers with (molecular) Schmidt numbers of $\mathcal{O}(10^3)$ (as in our example), β is of $\mathcal{O}(10^3)$, and therefore dominates over the logarithmic part in the wall-layer expression in Equation 13. This suggests, in accordance with available observations (see, e.g., Figure 1a in Lorke et al., 2003), that tracer concentrations are nearly constant across the turbulent bottom boundary layer, except for the thin DBL immediately adjacent to the sediment-water interface. As discussed in Section 3.2 above, the effect of this thin sublayer (not resolved in our simulations) is implicitly taken into account with the help of the transfer function β in Equation 17. The convergence of the numerical solutions toward the theoretical log-layer relations provides a rather strict test for the numerical implementation especially for the tracer profiles, for which vertical variations are very small.

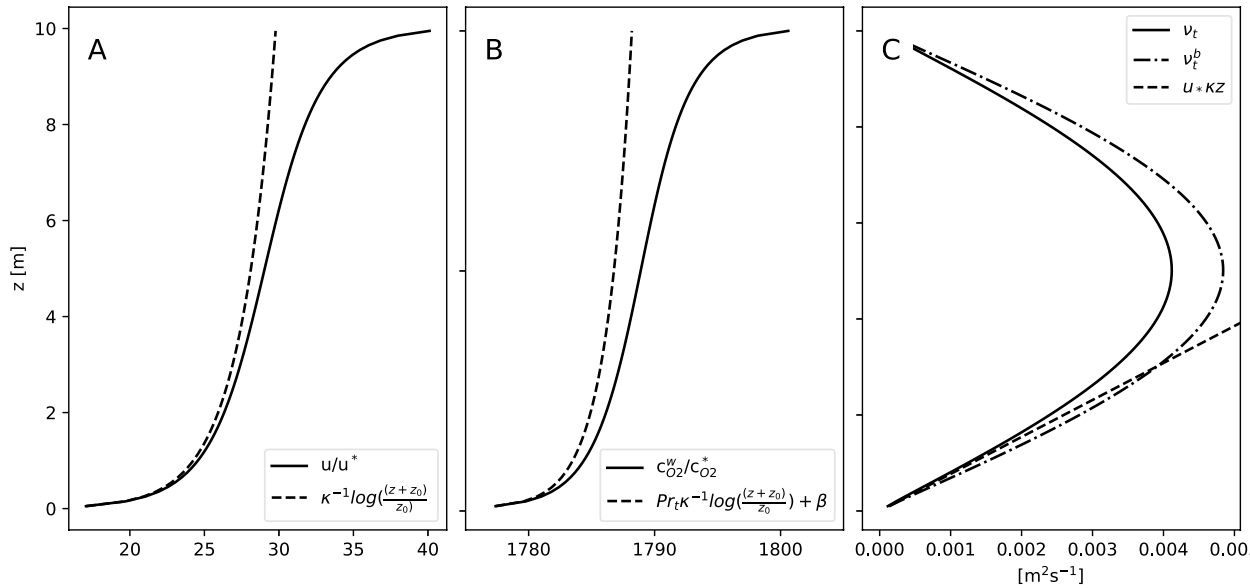

Figure 4. Non-dimensional steady-state profiles of (a) velocity and (b) oxygen from numerical simulations and corresponding law-of-the-wall expressions in Equations A5 and 13, respectively. Panel (c) shows the simulated turbulent diffusivities of momentum and tracers (and the law-of-the-wall expression for momentum).

The corresponding steady-state tracer distributions in the benthic compartment are shown in Figure 5 (note that, for clarity, only the uppermost centimeter of the benthic layer is shown here). The oxygen profile for our reference case (orange line in Figure 5a) is characterized by a thin oxic layer of a few millimeters thickness, in which oxygen is directly consumed via the constant sink term $S_{O2} > 0$ (Figure 5c). This process is thought to represent aerobic heterotrophic activity in our model. Below this thin oxic layer, anaeorbic carbon degradation dominates, leading to the production of reduced compounds ($S_{OD} > 0$) that gradually diffusive upward. Inside the redoxcline region with overlapping oxygen and ODU gradients, ODUs diffusing upward away from their generation region are re-oxidized (Figure 5d), leading to another important oxygen sink inside the oxic layer. The turnover rates shown in Figure 5d are typically much larger than the aerobic respiration rate of $S_{O2} = 2 \times 10^{-4}$ mol kg^{-1} d^{-1}, indicating that, in our example, the reoxidation of reduced compounds dominates the total benthic oxygen demand. This is consistent with the finding that the oxygen penetration depth is much smaller than the value of $D_{O2} = \sqrt{2\nu_{O2} S_{O2} c^b_{O2}} \approx 13$ mm computed from the model of Bouldin (1968) for the case of purely aerobic respiration ($S_{O2} = \text{const.}$, $S_{OD} = 0$).

Figure 5d shows that smaller turnover time scales (larger k_t) result in a thinner and more pronounced redoxcline, inside which virtually all reduced compounds diffusing upward are consumed before reaching the sediment-water interface (Figure 5b). In this case, no ODUs will be able to escape from the benthic compartment. Vice-versa, for the largest turnover time scale (in blue), the redoxcline broadens and merges into the sediment-water interface. Part of the ODUs diffusing upward will therefore reach the interface and diffuse into the water column, where they are re-oxidized. In this situation, the oxygen flux into the sediment is not a reliable measure of total carbon degradation any more even after the system has become stationary.

6.2. Periodic Forcing

As near-bottom currents are often dominated by oscillating components induced by tides, internal waves, internal seiches in lakes, and other periodic motions, it is instructive to investigate the response of the benthic fluxes and concentrations with respect to periodic forcing. To this end, we prescribe a barotropic pressure gradient in the momentum Equation 2 exactly such that the velocity at the surface follows a sinusoidal variation of the form $u(z = H, t) = U \sin(2\pi t/T_p)$, where T_p is the forcing period and U the velocity amplitude. All other parameters correspond to those compiled in Table 1, except for the wind stress τ^s_x, which is set to zero here. All simulations discussed in the following are analyzed after fully periodic conditions have been reached.

In our first example, we use $T_p = 24$ hr and $U = 0.1$ m s^{-1}, which can be thought of as representing, for example, diurnal internal seiching motions in a lake or diurnal tidal currents in the ocean (other forcing periods will be

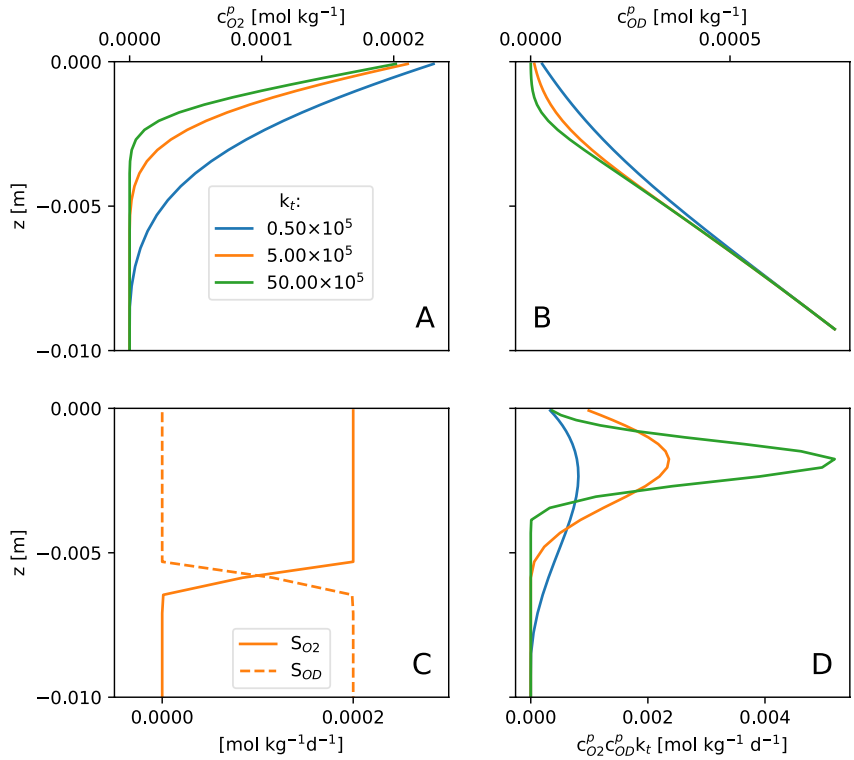

Figure 5. Steady-state benthic profiles of (a) oxygen concentrations, (b) oxygen demand unit (ODU) concentrations, (c) ODU and oxygen source and sink terms, and (d) turnover term appearing in Equations 10 and 11. Line colors correspond to different values of the turnover constant k_t as indicated in panel (a). Note that only the upper part of the benthic compartment with a total thickness of 0.05 m is shown here.

studied below). Figure 6a shows that friction effects reduce the near-bottom current speeds down to approximately 0.05 m s^{-1}, which is typical for many marine and limnic systems.

The signature of the periodic bottom currents is directly imprinted in the oxygen penetration depth and the benthic oxygen concentrations (Figure 6b), where concentrations at the sediment-water interface vary by more than a factor of 4 between periods with lowest and highest current speeds. As oxygen concentrations in the water column are close to saturation throughout the simulation period (not shown), this variability is largely explained by variations in the DBL thickness, illustrating the crucial impact of the physical forcing. Figure 6c shows that the thickness δ_{O2} of the DBL increases from values below 1 mm during periods with maximum current speeds by more than a factor of 10 around current reversal. This variability of δ_{O2} is directly reflected in the benthic fluxes (Figure 6d) that nearly collapse when bottom currents reach their minimum values. Overall, these results are strikingly similar to observations (Brand et al., 2008; Bryant, Lorrai, et al., 2010; Lorke et al., 2003) and idealized (uncoupled) simulations (Brand et al., 2009) of temporal variations of oxygen fluxes in different lakes.

It should be noted that the benthic fluxes shown Figure 6c are not symmetrically distributed about the points of current reversal, with consistently stronger fluxes observed after current reversal, respectively. As variations in δ_{O2} are almost perfectly symmetric in time, this effect cannot be explained by the physical forcing. The more likely reason is the oxygen deficit that builds up around current reversal (Figure 6b). As soon as current speeds start increasing again, and the diffusive sublayer becomes a less important bottle neck, this deficit is compensated by both an increased flux of oxygen into the sediment and an enhanced export of ODUs into the water column. Both effects are clearly visible in Figure 6d.

Figure 7 shows the effect of different forcing periods in the range T_p = 0.5–4 days, which includes the important semi-diurnal and diurnal tides, near-inertial motions, and the typical frequency bands for shelf-waves in the ocean and internal seiching motions in lakes. All other parameters remain unchanged. After scaling the time t with the forcing period T_p, the curves for the DBL thicknesses (Figure 7a) nearly collapse with significant differences confined to short periods before and after current reversal, pointing at friction-induced phase shifts of

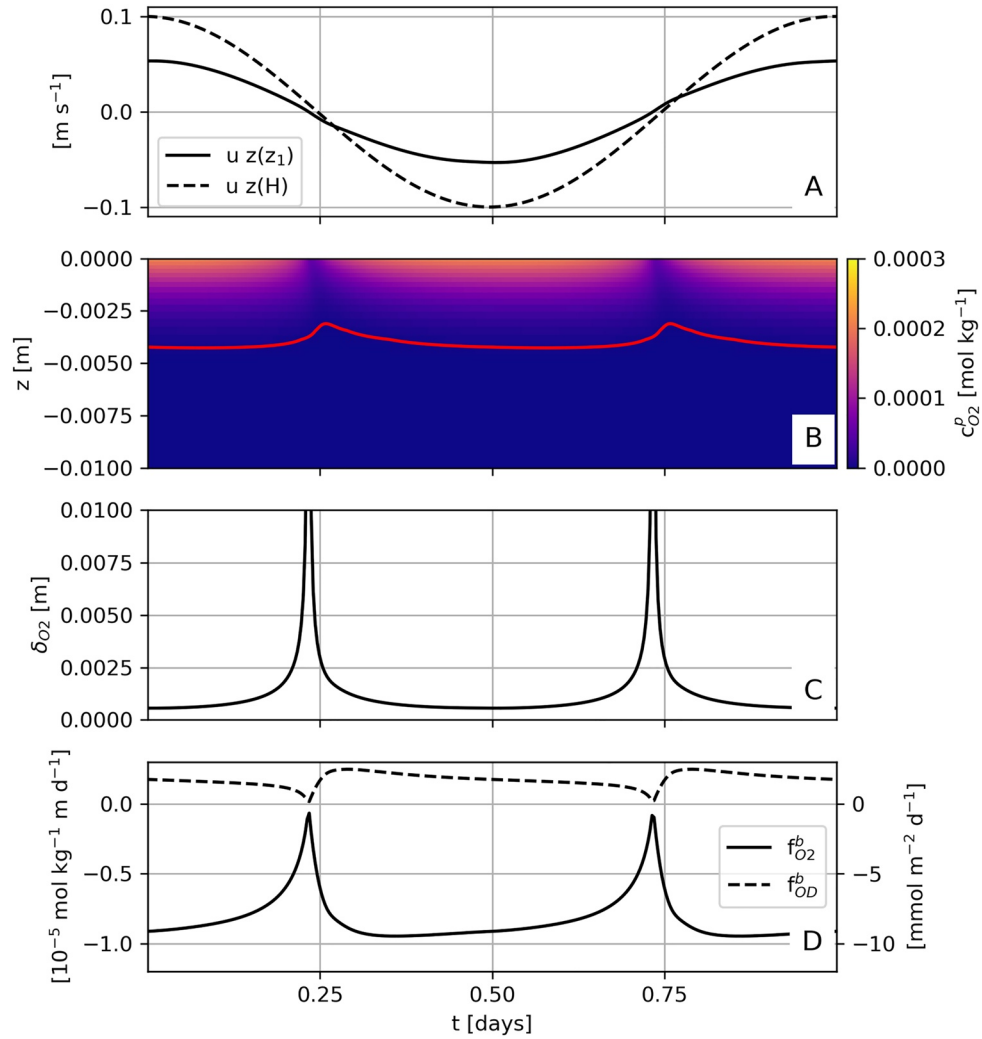

Figure 6. Temporal variability of (a) surface and near-bottom velocities, (b) benthic oxygen concentrations, (c) diffusive boundary layer thickness, and (d) oxygen and oxygen demand unit fluxes across the sediment-water interface. The red line in panel (b) indicates the oxygen penetration depth, here defined as the depth at which oxygen concentrations have decayed to 1% of the saturation concentration. Solutions are shown for fully periodic conditions. The origin of the time axis is arbitrary.

the near-bottom velocities. This is contrasted by the oxygen penetration depths (Figure 7b), which show a clear dependency on T_p especially after current reversal. Cases with larger T_p show a more pronounced reduction of the oxygen penetration depth, indicating that a larger oxygen deficit has accumulated during the longer (in dimensional units) current reversal period where interfacial oxygen fluxes are blocked by the DBL.

Figure 7c shows that the asymmetry in the interfacial oxygen fluxes discussed above is also found for all other forcing periods, with the strongest fluxes again occurring after current reversal, respectively. After the reversal, the magnitude of the oxygen fluxes shows a clear trend to decrease for increasing T_p, which at first glance is somewhat counter-intuitive in view of the larger oxygen debt accumulated for larger T_p. Two reasons explain this behavior. First, as shown in Figure 7a, for small T_p the DBL shrinks more quickly (in non-dimensional units) after current reversal, allowing the oxygen fluxes to recover more rapidly. Second, the reduction of the oxygen penetration depth for larger T_p allows ODUs to reach the sediment-water interface and escape into the water column (Figure 7c). This implies that less oxygen is required to re-oxidize reduced compounds inside the benthic layer, which is reflected in the reduced oxygen fluxes for these cases. Overall, however, it is clear from Figure 7c that the amplitudes of the temporal variations of the fluxes are comparable for all periods, which is consistent with results from a more advanced (although not fully coupled) benthic model by Brand et al. (2009).

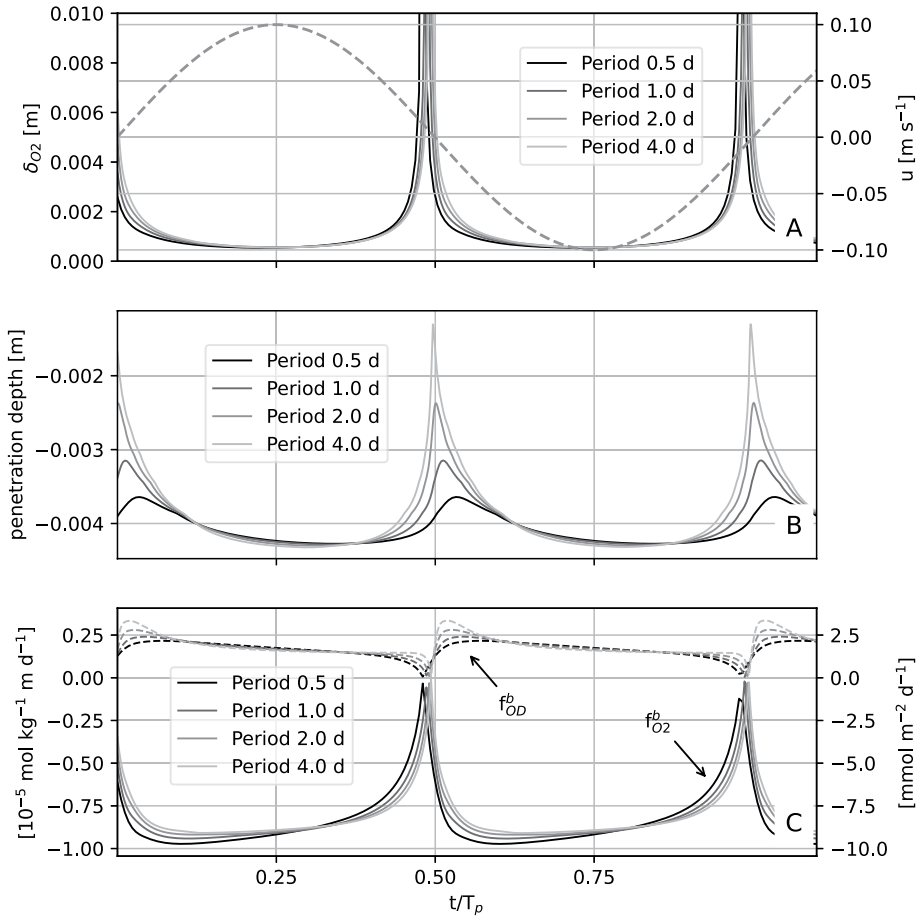

Figure 7. Periodic evolution of (a) diffusive boundary layer thickness, (b) oxygen penetration depth, and (c) oxygen and oxygen demand unit fluxes across the sediment-water interface for different forcing periods after fully periodic conditions are reached (all other parameters as in Figure 6). The dashed line in panel (a) indicates the prescribed sinusoidal velocity at the surface. Time has been non-dimensionalized by the forcing period T_p.

6.3. Stratification Effects

In our final example, we study the added complexity introduced by the feedbacks between stratification, atmospheric forcing, and turbulence, and their impact on oxygen dynamics. We build up on the simulation from the previous section by adding a sharp thermocline at 7 m depth, thus creating a 3 m thick bottom boundary layer (BBL) that is largely isolated from the surface region of our 10 m deep water column (Figure 8a). We use the same 24-hr periodic forcing as in the previous section but now also prescribe an initially weak wind stress of $\tau^s_x = 10^{-3}$ Pa, approximately corresponding to 1 m s^{-1} winds, to maintain turbulence in the surface layer. The water column is initialized with zero ODU concentrations and oxygen concentrations of $c^w_{O2} = 1.5 \times 10^{-4}$ mol kg^{-1}, which is half the saturation concentration. As before, the surface oxygen flux is adjusted to keep oxygen concentrations at the surface exactly at the saturation level of $c^w_{O2} = 3 \times 10^{-4}$ mol kg^{-1}. The porewater was initialized with a constant ODU concentration of 1.5×10^{-3} mol kg^{-1} and zero oxygen.

The blocking effect of the density interface on the turbulent transport is immediately evident from Figure 8a: while oxygen concentrations in the well-mixed surface layer quickly approach saturation levels on a time scale of day, they gradually decrease toward zero in the BBL. After $t = 32$ days, the wind stress is suddenly increased to $\tau^x_s = 4 \times 10^{-2}$ Pa to simulate the effect of a wind event. The resulting increase in surface-layer turbulence leads to a quick erosion of the pycnocline and a ventilation of the entire water column down to the bottom within approximately 30 hr (Figure 8a).

During the initial period before the wind event, the uppermost part of the benthic layer shows periodic fluctuations in oxygen concentrations and penetration depths (Figure 8b), which, similar to the unstratified case, are

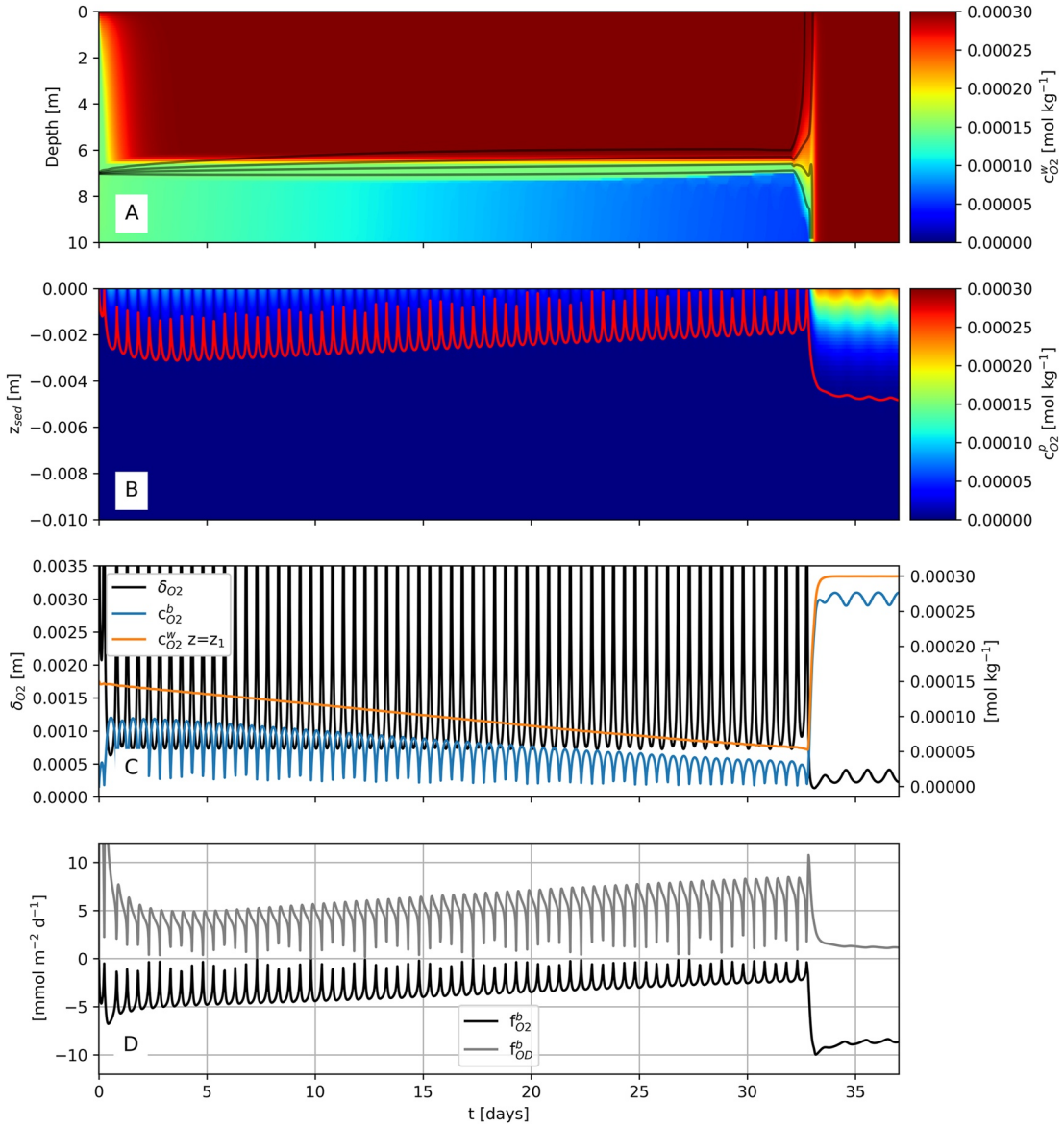

Figure 8. Evolution of (a) pelagic oxygen concentrations, isopycnals in intervals of 0.5 kg m^{-3} in black, (b) benthic oxygen concentrations, (c) diffusive boundary layer thickness (black), oxygen concentrations in center of lowest grid cell (orange) and at the sediment-water interface (blue), and (d) sediment-water fluxes of oxygen (black) and oxygen demand units (dashed). The red line in (b) denotes the oxygen penetration depth as in Figure 6b.

imposed by variations in the DBL thickness (black line in Figure 8c). These fluctuations are now, however, modulated by a gradual decay that reflects the decreasing oxygen concentrations in the BBL. As a result, the sediment-water fluxes (Figure 8d) show a gradual transition from benthic oxygen uptake to a situation where reduced compounds (ODUs) are primarily exported from the sediments toward the BBL. Both factors lead to decreasing oxygen concentrations in the BBL, either by oxygen loss toward the sediment or by re-oxidation of reduced compounds diffusing out of the sediment.

After the onset of the wind event on day 32, benthic oxygen concentrations quickly recover (Figure 8b), ODU interface fluxes collapse, and the benthic oxygen demand is satisfied almost completely again by the transport of oxygen across the sediment-water interface (Figure 8d). It is interesting to note that, while both the near-bottom oxygen concentration c_1 and the interface concentration c^b strongly increase after the onset of the wind event (orange and blue lines in Figure 8c), their difference $c_1 - c^b$ remains comparable. According to (16), the strongly increasing oxygen concentrations after the wind event can thus be largely attributed to the reduction of the

diffusive sublayer thickness induced by stronger near-bottom turbulence (Figure 8c), highlighting once more the importance of hydrodynamic effects.

7. Discussion and Conclusions

Most previous investigations of the impact of DBL variations on sediment-water solute exchange (e.g., Brand et al., 2009; Glud et al., 2007; Kelly Gerreyn et al., 2005) have focused solely on the benthic modeling component, forced by prescribed pelagic solute concentrations and DBL thicknesses. While this approach provided valuable insights into the adjustment of the benthic biogeochemistry and fluxes in response to DBL variations, it obviously eliminates any benthic-pelagic feedbacks. Here, extending these previous studies, we investigated such feedbacks based on a fully coupled benthic-pelagic modeling approach, where near-bottom solute concentrations are derived from a pelagic biogeochemical model, and DBL fluctuations are computed as a function of (modeled) near-bottom hydrodynamics.

In our simple benthic biogeochemical model, the rates of aerobic respiration, S_{O2}, and production of reduced compounds, S_{OD}, are kept constant, thus assuming a fixed carbon oxidation rate. While the instantaneous sediment-water fluxes may show strong fluctuations due to variations in the DBL thickness in this model, the long-term average benthic oxygen demand remains constant and unaffected by the presence of the DBL. This is qualitatively similar to the simple analytical model used by Jørgensen and Boudreau (2001, page 232) to illustrate that the production of reduced compounds (sulfide in their case) determines the benthic oxygen demand under stationary conditions if aerobic respiration is ignored ($S_{O2} = 0$). The same behavior is also found in more advanced biogeochemical models discussed, for example, in Glud (2008) and Glud et al. (2007). In this context, it is, however, important to note that total benthic oxygen demand, including both aerobic respiration and reoxidation of reduced compounds, can be satisfied by either a flux of oxygen into the sediments or by a release of reduced compounds from the sediments into the bottom boundary layer. One important result of our study (see Section 6.3) therefore is that the transition between these two regimes is determined by near-bottom oxygen concentrations and hydrodynamic control that are part of a feedback mechanism that connects decreasing oxygen concentrations in the bottom boundary layer to increasing fluxes of reduced compounds out of the sediment. A release of reduced compounds into the water column was also reported by Brand et al. (2009), who found that in some of their simulations up to 45% of the Fe^{2+} and 95% of the Mn^{2+} produced in the lower part of benthic layer escaped into the overlying water column. Their model was, however, forced by prescribed concentrations at the upper edge of the DBL, which did not allow for benthic-pelagic feedbacks.

The possibility of our model to accumulate a benthic "oxygen debt" (Glud, 2008), in form of either small benthic oxygen concentrations or large concentrations of reduced compounds, introduces the possibility for phase shifts in the benthic response to periodic hydrodynamic forcing, for example, due to tides or internal-wave motions. Longer forcing periods were found to induce a larger oxygen debt at the point of flow reversal, when benthic oxygen fluxes collapse due to the blocking effect of the DBL. This is reflected in a larger release of reduced compounds into the water column shortly after the flow reversal, when the DBL becomes thinner again, providing less resistance (Figure 7c). Vice-versa, shortly before the flow reversal, benthic oxygen fluxes increase for increasing forcing periods to compensate for the increasing benthic oxygen debt. Therefore, the ratio of the long-term averages of the fluxes of oxygen and reduced compounds is a function of the forcing period, or, more generally, of the "history" of the benthic layer. This implies that the oxygen flux, even if averaged over a long period, is generally not a reliable measure of the total carbon respiration rate. Overall, we find that hydrodynamic control of benthic fluxes is particularly relevant on time scale of days, corresponding to seiching motions in lakes, tides, and the typical variability of atmospheric forcing.

Finally, we want to point out that our numerical methods were designed from the outset to integrate with existing hydrodynamic models—here, GOTM—to perform fully coupled benthic-pelagic simulations. This places additional constraints on the type of integration methods that can be used. Hydrodynamic models generally use a constant, small integration time step (nearly always < 1 hr, often on the order of minutes), which coupled biogeochemical models must use as well to reliably represent hydrodynamic coupling feedbacks. While it is conceivable to employ adaptive, implicit schemes for the biogeochemistry to bridge such a single time step, the additional computational cost of such schemes generally only becomes worthwhile at much larger time steps. We also showed that the consistent integration of hydrodynamic effects on sediment-water exchange in a coupled modeling system poses a number of numerical challenges that carefully have to be taken into account. Our

numerics employ a newly developed Patankar-type (Patankar, 1980) limiter of the sediment-water fluxes to insure non-negative concentrations at, and mass conservations across, the sediment-water interface. This method is fully conservative, guarantees positive solute concentrations, and allows, in principle, for different time steps for the pelagic and benthic components, respectively. Alternatively, as briefly mentioned in Section 4, the benthic and pelagic compartments could also be combined into a single matrix system, which would avoid time splitting errors but would not permit different time steps for the two compartments any more. We also showed that the transfer coefficients for the sediment water fluxes have to be consistent with the theoretical predictions for the logarithmic near-bottom layer for tracers to avoid a grid-dependence of the results. This plays an especially important role for tracers with small Schmidt numbers, as discussed in a related context (ice-ocean heat fluxes) by Burchard et al. (2022).

The focus of this study was on a consistent parameterization and numerical implementation of hydrodynamic control effects, and on the identification of the basic feedback mechanisms in coupled benthic-pelagic systems with the help of a very elementary biogeochemical model. Ongoing work will concentrate on the implementation of more advanced biogeochemical descriptions (e.g., Brand et al., 2009; Glud et al., 2007; Soetaert et al., 1996a, 1996b), and on their integration in three-dimensional modeling systems to reveal the spatial structure of DBL variations in real marine and limnic systems, and identify hotspots and conditions, for which hydrodynamic control effects are especially relevant.

Appendix A: Turbulence Modeling

The turbulent diffusivities of momentum and tracers are computed from expressions of the form

$$\nu_t = c_\mu\left(\bar{N},\bar{M}\right)\frac{k^2}{\varepsilon}, \quad \nu_t^b = c_\mu^b\left(\bar{N},\bar{M}\right)\frac{k^2}{\varepsilon}, \tag{A1}$$

where k denotes the turbulent kinetic energy (TKE) and ε the turbulence dissipation rate. The stability functions c_μ and c_μ^b are derived from an algebraic version of the second-moment turbulence closure model described in detail in Umlauf and Burchard (2005), using the model parameters suggested by Canuto et al. (2001). These functions depend on the (non-dimensional) buoyancy and shear frequencies, $\bar{N} = Nk/\varepsilon$ and $\bar{M} = Mk/\varepsilon$, where N is the buoyancy frequency (defined above) and $M = \sqrt{(\partial u/\partial z)^2 + (\partial v/\partial z)^2}$ the magnitude of the vertical shear.

The TKE and the dissipation rate are derived from prognostic transport equations of the form

$$\frac{\partial k}{\partial t} = \frac{\partial}{\partial z}\left(\frac{\nu_t}{\sigma_k}\frac{\partial k}{\partial z}\right) + P + G - \varepsilon, \tag{A2}$$

$$\frac{\partial \varepsilon}{\partial t} = \frac{\partial}{\partial z}\left(\frac{\nu_t}{\sigma_\varepsilon}\frac{\partial \varepsilon}{\partial z}\right) + \frac{\varepsilon}{k}(c_1 P + c_3 G - c_2\varepsilon), \tag{A3}$$

where c_1, c_2, c_3, σ_k, and σ_ε are model parameters listed in Umlauf and Burchard (2005). The turbulence shear production P and the buoyancy production G appearing on the right hand sides of Equations A2 and A3 are defined as

$$P = \nu_t M^2, \quad G = -\nu_t^b N^2. \tag{A4}$$

Bottom boundary conditions for Equations A2 and A3 are derived based on the assumption that the lowermost grid cell is located inside the logarithmic bottom layer, typically requiring an $\mathcal{O}(0.1-1)$ m numerical resolution near the bottom. Both the Reynolds stress and the TKE are approximately constant in this logarithmic region, and the dissipation rate decreases inversely with the wall distance, $\varepsilon = u_*^3/(\kappa(z+z_0))$, as discussed, for example, in Pope (2000). Based on these expressions, consistent boundary conditions of the form $\partial k/\partial z = 0$ and $\varepsilon = u_*^3/(\kappa z_0)$ at $z = 0$ can be derived (see Umlauf & Burchard, 2005).

Using these boundary conditions, it is straightforward to show that the velocity profile follows the well-known logarithmic distribution,

$$\frac{|\boldsymbol{u}|}{u_*} = \frac{1}{\kappa}\ln\frac{z+z_0}{z_0}, \tag{A5}$$

where $\kappa = 0.416$ is the value of the von Kármán constant predicted by our model (see Umlauf & Burchard, 2003). The predicted turbulent diffusivity of momentum,

$$\nu_t = \kappa u_*(z + z_0), \tag{A6}$$

increases linearly with distance from the bottom in the logarithmic layer, consistent with dimensional arguments and experiments (Pope, 2000). Similarly, it can be shown that the tracer diffusivity predicted by our turbulence model is:

$$\nu_t^b = Sc_t^{-1}\kappa u_*(z + z_0). \tag{A7}$$

While the turbulent Schmidt number, $Sc_t = \nu_t/\nu_t^b$, will be, in general, a function of the non-dimensional shear and stratification parameters $\bar{N}$ and $\bar{S}$ according to Equation A1, it can be shown that in the logarithmic bottom layer, Sc_t converges toward a constant value of order 1 (here: $Sc_t = 0.85$, see Canuto et al., 2001). Analogous to Equation A6, therefore, also the tracer diffusivity in Equation A7 shows a linear variability in the logarithmic bottom region.

Appendix B: Transfer Coefficients for Tracers

Similarly to Equation A5, it can be shown that also the logarithmic tracer profile in Equation 13 is an exact solution of our model equations, however, with the additional complication that the unknown transfer function β has to be prescribed based on the roughness properties of the bottom and the molecular Schmidt number Sc of the fluid. In their pioneering work on turbulent wall exchange, Kader and Yaglom (1972) and Yaglom and Kader (1974) suggested expressions for β for fluids with various Schmidt numbers, considering the special cases of hydrodynamically smooth and rough surfaces, respectively.

For the case of a hydrodynamically smooth bottom, Kader (1981) summarized results originally derived by Kader and Yaglom (1972) and suggested a revised expression for the function β, which, after converting to our notation, can be written as

$$\beta = \left(3.85Sc^{\frac{1}{3}} - 1.3\right)^2 + Sc_t\left(\frac{\ln Sc}{\kappa} - B\right) \quad \text{for } z_0^+ < 0.1, \tag{B1}$$

For tracers with a large Schmidt number ($Sc \to \infty$), Equation B1 converges to

$$\beta = 14.8Sc^{2/3} \quad \text{for } z_0^+ < 0.1, \tag{B2}$$

which is a useful approximation for the most relevant tracers like oxygen, dissolved trace gases, and nutrients with $Sc = \mathcal{O}(10^3)$. Subsequent studies have confirmed this simplified relationship for large Sc with only small modifications of the constant model factor and the 2/3 power-law dependency on Sc (see, e.g., Dade, 1993; Santschi et al., 1991; Shaw & Hanratty, 1977, and the references therein). For these reasons, all simulations in this manuscript will be based on Equation B2.

For a hydrodynamically rough bottom $\left(z_0^+ > 3\right)$, Yaglom and Kader (1974, see their Equation 13) suggested an expression for β that essentially depends on the non-dimensional bottom roughness, z_0^+, and the Schmidt number, Sc. Taking into account their different definition of β, and converting to our notation, their expression yields:

$$\beta = 0.55\exp\left(\kappa B'/2\right)\left(z_0^+\right)^{\frac{1}{2}}\left(Sc^{\frac{2}{3}} - 0.2\right) - Sc_t B' + 9.5 \quad \text{for } z_0^+ > 3, \tag{B3}$$

which condenses to $\beta = 0.55\exp(\kappa B'/2)\left(z_0^+\right)^{1/2}Sc^{\frac{2}{3}}$ for large Schmidt numbers. All of the above expressions are included in the numerical code.

Data Availability Statement

All simulations were carried out with the General Ocean Turbulence Model (GOTM, https://gotm.net), coupled to the Framework for Aquatic Biogeochemical Models (FABM, https://github.com/fabm-model) and extended by a benthic module developed for the purpose of this study. The source code (Bruggeman et al., 2023) and the setup files (Holtermann & Umlauf, 2023) are available on Zenodo.

Acknowledgments
The authors thank the three anonymous reviewers for their insightful comments that helped to improve the manuscript. P. Holtermann and L. Umlauf are grateful for the support by the Leibniz Association (WGL) provided in the framework of the project FORMOSA (Grant K227/2019). The work of K. Klingbeil was funded by the German Research Foundation (DFG) through subproject M5 of the Collaborative Research Center TRR 181 "Energy Transfer in Atmosphere and Ocean" (project number 274762653). R. Schwefel was supported by the Swiss National Science Foundation (SNF) Grants 200021_146652 and 200020_165517. J. Bruggeman was supported by the Marine Ecosystems Research Programme (NE/L003066/1), funded by the UK Natural Environment Research Council (NERC) and Department for Environment Food and Rural Affairs (Defra). Open Access funding enabled and organized by Projekt DEAL.

References

Berg, P., Huettel, M., Glud, R. N., Reimers, C. E., & Attard, K. M. (2022). Aquatic eddy covariance: The method and its contributions to defining oxygen and carbon fluxes in marine environments. *Annual Review of Marine Science*, *14*(1). https://doi.org/10.1146/annurev-marine-042121-012329

Berg, P., Røy, H., Janssen, F., Meyer, V., Jørgensen, B. B., Huettel, M., & De Beer, D. (2003). Oxygen uptake by aquatic sediments measured with a novel non-invasive eddy-correlation technique. *Marine Ecology Progress Series*, *261*, 75–83. https://doi.org/10.3354/meps261075

Boudreau, B. P. (1997). *Diagenetic models and their implementation* (Vol. 505). Springer Berlin.

Bouldin, D. R. (1968). Models for describing the diffusion of oxygen and other mobile constituents across the mud-water interface. *Journal of Ecology*, *56*(1), 77–87. https://doi.org/10.2307/2258068

Brand, A., Dinkel, C., & Wehrli, B. (2009). Influence of the diffusive boundary layer on solute dynamics in the sediments of a seiche-driven lake: A model study. *Journal of Geophysical Research*, *114*(G1), G01010. https://doi.org/10.1029/2008JG000755

Brand, A., McGinnis, D. F., Wehrli, B., & Wüest, A. (2008). Intermittent oxygen flux from the interior into the bottom boundary of lakes as observed by eddy correlation. *Limnology and Oceanography*, *53*(5), 1997–2006. https://doi.org/10.4319/lo.2008.53.5.1997

Brigolin, D., Lovato, T., Rubino, A., & Pastres, R. (2011). Coupling early-diagenesis and pelagic biogeochemical models for estimating the seasonal variability of N and P fluxes at the sediment–water interface: Application to the northwestern Adriatic coastal zone. *Journal of Marine Systems*, *87*(3), 239–255. https://doi.org/10.1016/j.jmarsys.2011.04.006

Bruggeman, J., & Bolding, K. (2014). A general framework for aquatic biogeochemical models. *Environmental Modelling and Software*, *61*, 249–265. https://doi.org/10.1016/j.envsoft.2014.04.002

Bruggeman, J., Klingbeil, K., & Holtermann, P. L. (2023). GOTM/FABM source codes with hydrodynamically controlled benthic-pelagic coupled oxygen model [Software]. Zenodo. https://doi.org/10.5281/zenodo.7950383

Bryant, L. D., Lorrai, C., McGinnis, D. F., Brand, A., Est, A. W., & Little, J. C. (2010). Variable sediment oxygen uptake in response to dynamic forcing. *Limnology and Oceanography*, *55*(2), 950–964. https://doi.org/10.4319/lo.2010.55.2.0950

Bryant, L. D., McGinnis, D. F., Lorrai, C., Brand, A., Little, J. C., & Wüest, A. (2010). Evaluating oxygen fluxes using microprofiles from both sides of the sediment-water interface. *Limnology and Oceanography*, *8*(11), 610–627. https://doi.org/10.4319/lom.2010.8.0610

Burchard, H., Bolding, K., Jenkins, A., Losch, M., Reinert, M., & Umlauf, L. (2022). The vertical structure and entrainment of subglacial melt water plumes. *Journal of Advances in Modeling Earth Systems*, *14*(3), e2021MS002925. https://doi.org/10.1029/2021MS002925

Butenschön, M., Clark, J., Aldridge, J. N., Allen, J. I., Artioli, Y., Blackford, J., et al. (2016). ERSEM 15.06: A generic model for marine biogeochemistry and the ecosystem dynamics of the lower trophic levels. *Geoscientific Model Development*, *9*(4), 1293–1339. https://doi.org/10.5194/gmd-9-1293-2016

Calmet, I., & Magnaudet, J. (1997). Large-eddy simulation of high-schmidt number mass transfer in a turbulent channel flow. *Physics of Fluids*, *9*(2), 438–455. https://doi.org/10.1063/1.869138

Canuto, V. M., Howard, A., Cheng, Y., & Dubovikov, M. S. (2001). Ocean turbulence. Part I: One-point closure model—momentum and heat vertical diffusivities. *Journal of Physical Oceanography*, *31*(6), 1413–1426. https://doi.org/10.1175/1520-0485(2001)031<1413:otpiop>2.0.co;2

Dade, W. B. (1993). Near-bed turbulence and hydrodynamic control of diffusional mass transfer at the sea floor. *Limnology and Oceanography*, *38*(1), 52–69. https://doi.org/10.4319/lo.1993.38.1.0052

Feistel, R. (2012). TEOS-10: A new international oceanographic standard for seawater, ice, fluid water, and humid air. *International Journal of Thermophysics*, *33*(8–9), 1335–1351. https://doi.org/10.1007/s10765-010-0901-y

Fennel, K., Hu, J., Laurent, A., Marta-Almeida, M., & Hetland, R. (2013). Sensitivity of hypoxia predictions for the northern Gulf of Mexico to sediment oxygen consumption and model nesting. *Journal of Geophysical Research: Oceans*, *118*(2), 990–1002. https://doi.org/10.1002/jgrc.20077

Garcia, H. E., & Gordon, L. I. (1992). Oxygen solubility in seawater: Better fitting equations. *Limnology and Oceanography*, *37*(6), 1307–1312. https://doi.org/10.4319/lo.1992.37.6.1307

Glud, R. N. (2008). Oxygen dynamics of marine sediments. *Marine Biology Research*, *4*(4), 243–289. https://doi.org/10.1080/17451000801888726

Glud, R. N., Berg, P., Fossing, H., & Jørgensen, B. B. (2007). Effect of the diffusive boundary layer on benthic mineralization and O_2 distribution: A theoretical model analysis. *Limnology and Oceanography*, *52*(2), 547–557. https://doi.org/10.4319/lo.2007.52.2.0547

Gundersen, J. K., & Jorgensen, B. B. (1990). Microstructure of diffusive boundary layers and the oxygen uptake of the sea floor. *Nature*, *345*(6276), 604–607. https://doi.org/10.1038/345604a0

Hall, P. O. J., Anderson, L. G., Van der Loeff, M. M. R., Sundby, B., & Westerlund, S. F. G. (1989). Oxygen uptake kinetics in the benthic boundary layer. *Limnology and Oceanography*, *34*(4), 734–746. https://doi.org/10.4319/lo.1989.34.4.0734

Higashino, M., Gantzer, C. J., & Stefan, H. G. (2004). Unsteady diffusional mass transfer at the sediment/water interface: Theory and significance for SOD measurement. *Water Research*, *38*(1), 1–12. https://doi.org/10.1016/j.watres.2003.08.030

Holtappels, M., Glud, R. N., Donis, D., Liu, B., Hume, A., Wenzhöfer, F., & Kuypers, M. M. M. (2013). Effects of transient bottom water currents and oxygen concentrations on benthic exchange rates as assessed by eddy correlation measurements. *Journal of Geophysical Research: Oceans*, *118*(3), 1157–1169. https://doi.org/10.1002/jgrc.20112

Holtappels, M., Noss, C., Hancke, K., Cathalot, C., McGinnis, D. F., Lorke, A., & Glud, R. N. (2015). Aquatic eddy correlation: Quantifying the artificial flux caused by stirring-sensitive O_2 sensors. *PLoS One*, *10*(1), e0116564. https://doi.org/10.1371/journal.pone.0116564

Holtermann, P. L., & Umlauf, L. (2023). Channel flow with hydrodynamically controlled benthic-pelagic coupled oxygen fluxes [Software]. Zenodo. https://doi.org/10.5281/zenodo.7950866

Hondzo, M. (1998). Dissolved oxygen transfer at the sediment-water interface in a turbulent flow. *Water Resources Research*, *34*(12), 3525–3533. https://doi.org/10.1029/1998WR900009

Inoue, T., & Nakamura, Y. (2009). Effects of hydrodynamic conditions on sediment oxygen demand: Experimental study based on three methods. *Journal of Environmental Engineering*, *135*(11), 1161–1170. https://doi.org/10.1061/(asce)0733-9372(2009)135:11(1161)

Jørgensen, B. B., & Boudreau, B. P. (2001). Diagenesis and sediment-water exchange. In B. P. Boudreau & B. B. Jørgensen (Eds.), *The benthic boundary layer* (pp. 211–244). Oxford University Press.

Kader, B. A. (1981). Temperature and concentration profiles in fully turbulent boundary layers. *International Journal of Heat and Mass Transfer*, *24*(9), 1541–1544. https://doi.org/10.1016/0017-9310(81)90220-9

Kader, B. A., & Yaglom, A. M. (1972). Heat and mass transfer laws for fully turbulent wall flows. *International Journal of Heat and Mass Transfer*, *15*(12), 2329–2351. https://doi.org/10.1016/0017-9310(72)90131-7

Kelly-Gerreyn, B. A., Hydes, D. J., & Waniek, J. J. (2005). Control of the diffusive boundary layer on benthic fluxes: A model study. *Marine Ecology Progress Series*, *292*, 61–74. https://doi.org/10.3354/meps292061

Koopmans, D., Berg, P., Brunner, S., & Val Klump, J. (2021). Seiche- and storm-driven benthic oxygen uptake in a eutrophic freshwater bay determined with aquatic eddy covariance. *Freshwater Science*, *40*(2), 259–273. https://doi.org/10.1086/714542

Lemmen, C., Hofmeister, R., Klingbeil, K., Nasermoaddeli, M. H., Kerimoglu, O., Burchard, H., et al. (2018). Modular system for shelves and coasts (MOSSCO v1.0) – A flexible and multi-component framework for coupled coastal ocean ecosystem modelling. *Geoscientific Model Development*, *11*(3), 915–935. https://doi.org/10.5194/gmd-11-915-2018

Lorke, A., Müller, B., Maerki, M., & Wüest, A. (2003). Breathing sediments: The control of diffusive transport across the sediment—Water interface by periodic boundary-layer turbulence. *Limnology and Oceanography*, *48*(6), 2077–2085. https://doi.org/10.4319/lo.2003.48.6.2077

Millero, F. J., Feistel, R., Wright, D. G., & McDougall, T. J. (2008). The composition of standard seawater and the definition of the reference-composition salinity scale. *Deep Sea Research Part I: Oceanographic Research Papers*, *55*(1), 50–72. https://doi.org/10.1016/j.dsr.2007.10.001

Nakamura, Y., & Stefan, H. G. (1994). Effect of flow velocity on sediment oxygen demand: Theory. *Journal of Environmental Engineering*, *120*(5), 996–1016. https://doi.org/10.1061/(asce)0733-9372(1994)120:5(996)

Patankar, S. V. (1980). *Numerical heat transfer and fluid flow*. Hemisphere Publishing Corporation.

Pope, S. B. (2000). *Turbulent flows*. Cambridge University Press. https://doi.org/10.1017/CBO9780511840531

Radtke, H., & Burchard, H. (2015). A positive and multi-element conserving time stepping scheme for biogeochemical processes in marine ecosystem models. *Ocean Modelling*, *85*, 32–41. https://doi.org/10.1016/j.ocemod.2014.11.002

Radtke, H., Lipka, M., Bunke, D., Morys, C., Woelfel, J., Cahill, B., et al. (2019). Ecological ReGional Ocean Model with vertically resolved sediments (ERGOM SED 1.0): Coupling benthic and pelagic biogeochemistry of the south-western Baltic Sea. *Geoscientific Model Development*, *12*(1), 275–320. https://doi.org/10.5194/gmd-12-275-2019

Santschi, P. H., Anderson, R. F., Fleisher, M. Q., & Bowles, W. (1991). Measurements of diffusive sublayer thicknesses in the ocean by alabaster dissolution, and their implications for the measurements of benthic fluxes. *Journal of Geophysical Research*, *96*(C6), 10641–10657. https://doi.org/10.1029/91JC00488

Scalo, C., Piomelli, U., & Boegman, L. (2012). Large-eddy simulation of oxygen transfer to organic sediment beds. *Journal of Geophysical Research*, *117*(C6), C06005. https://doi.org/10.1029/2011JC007289

Schwefel, R., Hondzo, M., Wüest, A., & Bouffard, D. (2017). Scaling oxygen microprofiles at the sediment interface of deep stratified waters. *Geophysical Research Letters*, *44*(3), 1340–1349. https://doi.org/10.1002/2016GL072079

Shaw, D. A., & Hanratty, T. J. (1977). Turbulent mass transfer rates to a wall for large schmidt numbers. *AIChE Journal*, *23*(1), 28–37. https://doi.org/10.1002/aic.690230106

Soetaert, K., Herman, P. M. J., & Middelburg, J. J. (1996). Dynamic response of deep-sea sediments to seasonal variations: A model. *Limnology and Oceanography*, *41*(8), 1651–1668. https://doi.org/10.4319/lo.1996.41.8.1651

Soetaert, K., Herman, P. M. J., & Middelburg, J. J. (1996). A model of early diagenetic processes from the shelf to abyssal depths. *Geochimica et Cosmochimica Acta*, *60*(6), 1019–1040. https://doi.org/10.1016/0016-7037(96)00013-0

Sohma, A., Shibuki, H., Nakajima, F., Kubo, A., & Kuwae, T. (2018). Modeling a coastal ecosystem to estimate climate change mitigation and a model demonstration in Tokyo Bay. *Ecological Modelling*, *384*, 261–289. https://doi.org/10.1016/j.ecolmodel.2018.04.019

Steinberger, N., & Hondzo, M. (1999). Diffusional mass transfer at sediment-water interface. *Journal of Environmental Engineering*, *125*(2), 192–200. https://doi.org/10.1061/(asce)0733-9372(1999)125:2(192)

Umlauf, L., & Burchard, H. (2003). A generic length-scale equation for geophysical turbulence models. *Journal of Marine Research*, *61*(2), 235–265. https://doi.org/10.1357/002224003322005087

Umlauf, L., & Burchard, H. (2005). Second-order turbulence closure models for geophysical boundary layers. A review of recent work. *Continental Shelf Research*, *25*(7), 795–827. https://doi.org/10.1016/j.csr.2004.08.004

Umlauf, L., Burchard, H., & Bolding, K. (2005). *GOTM—Scientic documentation*, *63*, 279. https://doi.org/10.12754/MSR-2005-0063

Wang, J., Zhao, L., Fan, R., & Wei, H. (2016). Scaling relationships for diffusive boundary layer thickness and diffusive flux based on in situ measurements in coastal seas. *Progress in Oceanography*, *144*, 1–14. https://doi.org/10.1016/j.pocean.2016.03.001

Yaglom, A. M., & Kader, B. A. (1974). Heat and mass transfer between a rough wall and turbulent fluid flow at high reynolds and péclet numbers. *Journal of Fluid Mechanics*, *62*(3), 601–623. https://doi.org/10.1017/S0022112074000838